Vibration Reduction of a Semisubmersible Floating Wind Turbine using Optimized Tuned Mass and Tuned Inerter Dampers

Duncan Lambert

Thesis submitted to the Faculty of the
Virginia Polytechnic Institute and State University
in partial fulfillment of the requirements for the degree of

Masters of Science
in
Mechanical Engineering

Lei Zuo, Chair
Danesh K Tafti
David Ogden

May 5, 2023
Blacksburg, Virginia

Keywords: Offshore wind, Structural control, Tuned mass damper, Tuned inerter damper, Free decay, Regular wave

Vibration Reduction of a Semisubmersible Floating Wind Turbine using Optimized Tuned Mass and Tuned Inerter Dampers

Duncan Lambert

ABSTRACT

Over the past decade, offshore wind has positioned itself as one of the most promising renewable energy markets. While this field is currently dominated by fixed-bottom wind turbines located within a limited depth range, floating turbines are showing promise as a way to capture the more developed wind profiles available in deeper waters. Currently, the main challenge with floating offshore wind is that the systems experience larger ultimate loads compared to fixed bottom turbines. These larger loads are caused by the increased motion inherent with floating structures. This study looks to analyze the effects that traditional and inerter based structural control methods can have on vibration reduction of floating offshore wind turbines. Models are developed adding tuned mass dampers (TMD) and tuned inerter dampers (TID) into the three main columns of a semisubmersible platform. Results showed that for free decay tests, heave and pitch root mean square (RMS) values were reduced significantly by the addition of passive structural control. The inerter based structural control consistently outperformed traditional TMD and also allowed for similar performance with significantly reduced physical mass values. For regular wave excitation both control methods resulted in significant reductions to the heave and pitch RMS values compared to the baseline, with the TID outperforming the TMD . And for an irregular wave analysis, it was found that both control configurations were still able to provide meaningful reductions to the baseline model.

Vibration Reduction of a Semisubmersible Floating Wind Turbine using Optimized Tuned Mass and Tuned Inerter Dampers

Duncan Lambert

GENERAL AUDIENCE ABSTRACT

Over the past decade, offshore wind has positioned itself as one of the most promising renewable energy markets. While this field is currently dominated by fixed-bottom wind turbines located within a limited depth range, floating turbines are showing promise as a way to capture the more developed wind profiles available in deeper waters. Currently, the main challenge with floating offshore wind is that the systems experience larger loads compared to fixed bottom turbines. These larger loads are caused by the increased motion inherent with floating structures. This study looks to analyze the effects that traditional and enhanced motion reduction technology can have on floating offshore wind turbines. Models are developed adding the traditional and enhanced motion reduction technology into the three main columns of a semisubmersible platform. Results showed that for several different tests, the motion reduction technology has a positive effect on the turbines. For test dropping the system from a set height, the motion reduction technology allowed the system to come to rest much faster. Moreover, the enhanced technology performed better than the traditional technology. The same results were found when the system was excited by simulated waves.

Dedicated to Virginia Tech.

Contents

List of Figures

List of Tables

List of Abbreviations

BEM	Boundary element method
DOF	Degree of freedom
RMS	Root mean square
TID	Tuned inerter damper
TMD	Tuned mass damper

Chapter 1

Introduction

Many of the world's most pressing challenges today revolve around a need for clean energy. Whether the challenge is as straightforward as providing affordable energy to developing countries, or as complex as shifting the primary methods of energy consumption in an attempt to stabilize and reduce global warming, the focal point is still, a need for clean energy. The world's focus on tackling these challenges has intensified since the turn of the century, as evidenced by global agreements such as the Kyoto Protocol and the Paris Agreement. This focus has resulted in an exponential increase in funding, research, and growth in several different renewable energy fields. One such field that has experienced significant growth is wind energy, and more specifically offshore wind energy.

Offshore wind refers to the application of land based platforms in offshore regions through the use of fixed bottom foundations or floating platforms. As a whole, the offshore wind market has boomed in recent years, growing to a total installed capacity of over 50,000 MW over the last two decades. While this market is currently dominated by fixed-bottom wind turbines placed close to the shore, data shows that the use of floating platforms is expected to increase significantly over the next 5 years. This increase is due to the fact that wind speeds are much higher further offshore, in deeper water that is not suitable for fixed bottom designs. Also, the availability of sites for wind farms is greater further offshore. There are currently several floating platform designs used, though one in particular seems poised to dominate this market and that is the semisubmersible platform design. The semisubmersible platform is a concept originally developed by the University of Maine and is projected to support the vast majority of floating offshore wind farms by 2028. While this platform design currently outperforms other concepts, it still possesses many of the same shortcomings that characterize offshore floating wind turbines. The most severe shortcoming being that the semisubmersible platform experiences larger ultimate loads for many critical bending moments compared to land based or fixed bottom turbines. This increased loading comes from the fact that the semisubmersible platform is a moored structure and therefore can experience more motion than a fixed structure. In other words, more motion in critical degrees of freedom such as pitch and heave, means higher loads, which means a shorter lifespan. Though these larger motions could be remedied through the implementation of structural control, a concept that has been used to reduce motion in structures for over 100 years.

Structural control has largely been used to mitigate wind and earthquake induced motion in large buildings through the addition of motion reducing subsystems. The most famous of these subsystems is the passive tuned mass damper (TMD), that when tuned effectively can cancel out the majority of motion experienced by a building. Examples of buildings that utilize TMDs for motion reduction includes Taipei 101 in Taiwan and Park Tower in Chicago. In recent years, the inerter, a device that generates a force proportional to a relative acceleration, has begun to be integrated into structural control subsystems. The addition of the inerter has shown both an increase in performance and a reduction in the physical mass needed for structural control subsystems. Research into incorporating structural control into offshore floating wind platforms does exist, though is largely focused on adding a single fore-aft TMD into the nacelle or platform. Moreover, research into applying inerter based structural control into offshore floating wind platforms is even more limited. And at this time no study exists analyzing the effects of adding three traditional or inerter based structural control subsystems into the three primary columns of the semisubmersible platform design.

The contents of this thesis are organized as follows. Chapter 2 provides an extended introduction to the concepts covered in this thesis through a comprehensive literature review. Chapter 3 provides the derivation and verification of all TMD and inerter based wind turbine models used within this thesis. Chapter 4 presents and discusses the results of several free decay test optimizations, a regular wave optimization, and a subsequent irregular wave analysis. Lastly, chapter 5 states the key conclusions and introduces potential future work regarding this topic.

Chapter 2

Literature Review

2.1 Offshore Wind

The first offshore wind site was constructed in Sweden during the year of 1991. This pioneering venture consisted of one 220 kW wind turbine anchored to the seabed using a tripod foundation [5]. Since construction of this site, the offshore wind marked has grown exponentially, and as of 2023, is widely considered the most promising renewable energy resource. Harnessing wind energy began largely as a land based market, with the first energy producing wind turbine being constructed in Cleveland Ohio, back in 1881 [6]. But recently the focus has shifted to deploying wind turbines in offshore regions. The reason for the shift from onshore to offshore wind is likely due to lack of land available for onshore farms, smaller environmental impact caused by offshore wind, and strength of the wind resource available offshore [5]. The strength of this resource is highlighted by the map shown in Figure 2.1 [1]. This map shows the average wind speed across the U.S. at an elevation of 100 m above the surface. Darker colors indicate stronger wind speeds. While the continental U.S. does experience relatively large wind speeds in some places, particularly the Midwest. The strongest wind speeds occur consistently in offshore regions, particularly off the coast of California and the Northeast.

The growth of the offshore wind industry was discussed heavily in the 2022 Offshore Wind Market Report, published by NREL, and is summarized by Figure 2.2 [2]. Figure 2.2 shows

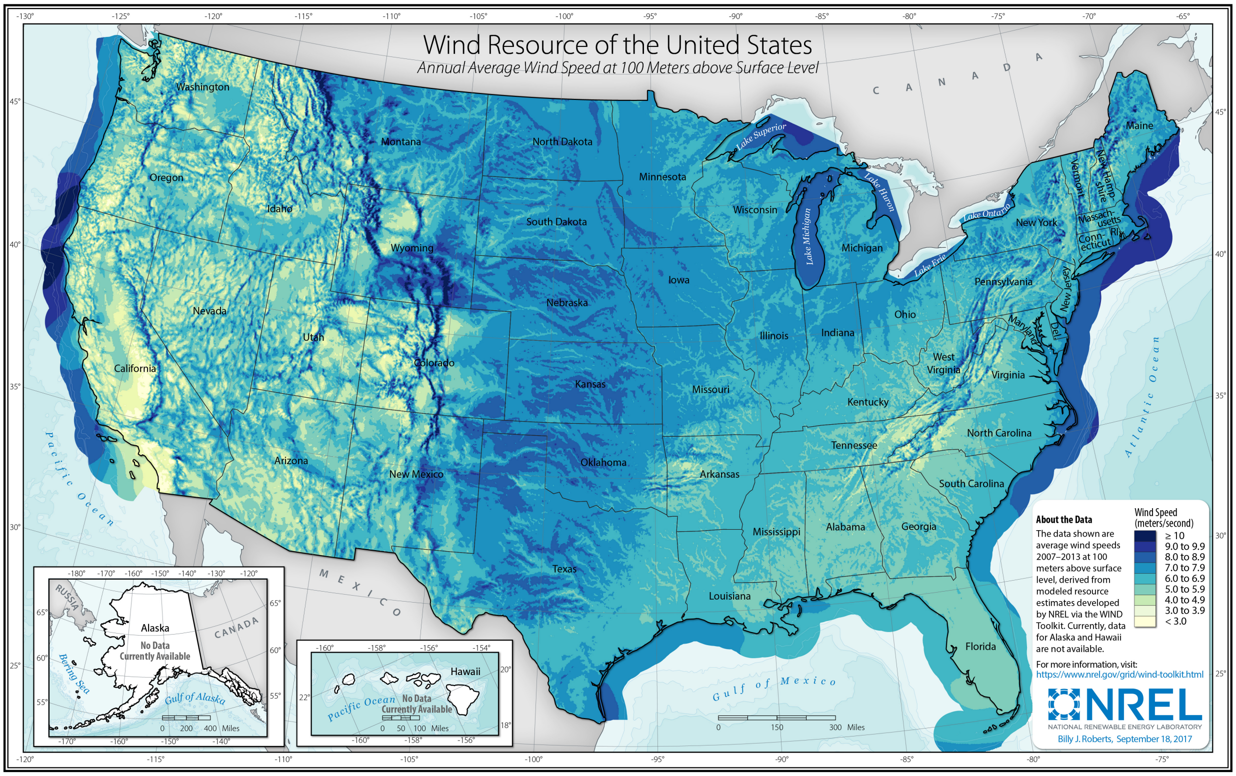

About the Data
The data shown are average wind speeds 2007–2013 at 100 meters above surface level, derived from modeled resource estimates developed by NREL via the WIND Toolkit. Currently, data for Alaska and Hawaii are not available.

For more information, visit: https://www.nrel.gov/grid/wind-toolkit.html

Billy J. Roberts, September 18, 2017

Figure 2.1: Wind resource for the U.S. at 100 m above surface level [1]

the cumulative installed capacity of offshore wind organized by country. The total installed capacity grew to 50,623 MW in 2021, which is up nearly 54% from the capacity of 32,906 MW reported in the 2021 edition of the Offshore Wind Market Report [7]. As of 2022, China leads all other countries in terms of cumulative installed capacity. This is because in 2021 China commissioned 13,790 MW more capacity than the rest of the world had installed in any previous year [2]. Other top contributors include the United Kingdom, which deployed 1,855 MW in 2021. It is also reported that 177,462 MW of new offshore wind farms have been announced through 2027, tripling the current capacity over the next 5 years. The overall trend of this data is a clear exponential boom in offshore wind that can only be expected to continue as the desire to reduce carbon emissions intensifies.

Traditionally, offshore wind has been focused on regions nearshore that utilize fixed bottom

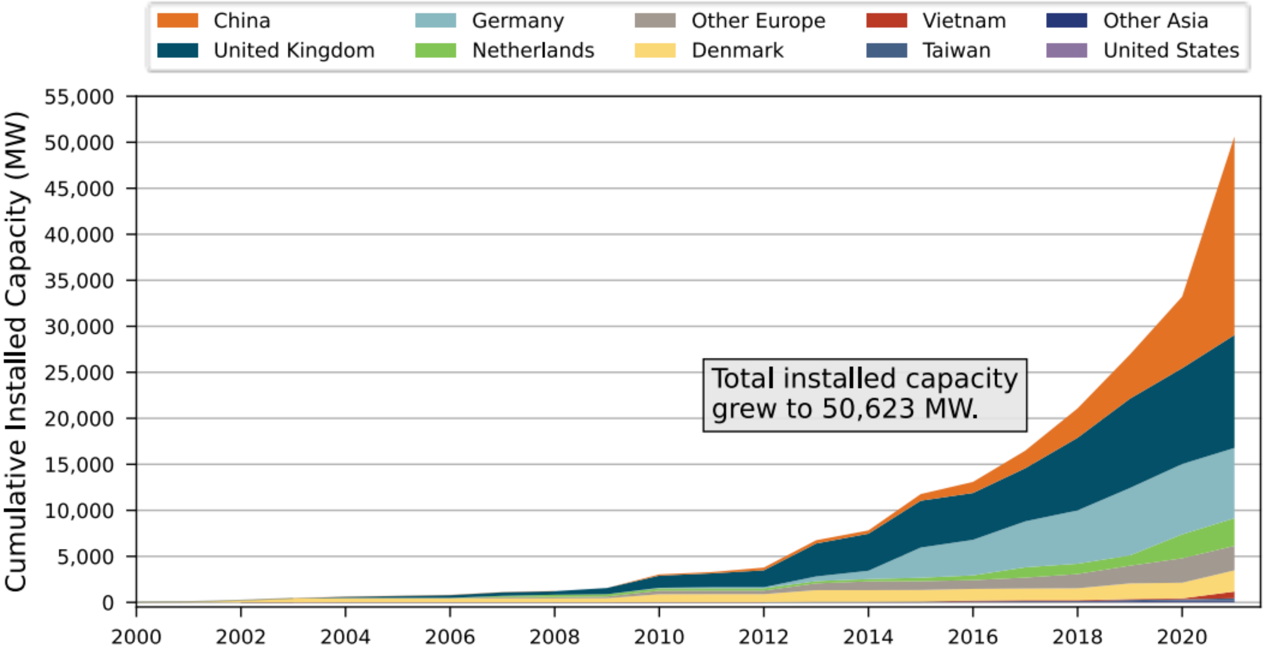

Figure 2.2: Cumulative installed capacity of offshore wind over time differentiated by country [2]

wind turbines. As the name suggests, this type of turbine is fixed directly to the seabed. More recently, deep water floating wind turbines have been the subject of increased interest. This is because wind power resources are more abundant in deeper water and the availability of deep water sites is much larger than nearshore sites [8]. Moreover, floating turbines likely have a smaller ecological footprint compared to fixed turbines [9]. Though several studies exist analyzing the ecological impact of the younger floating wind market as well [10] [11]. Figure 2.3 highlights the main differences between fixed and floating wind turbines [3]. The fixed platforms are typically viable in water depths less than 60 meters, while floating platforms are viable in water depths greater than 60 meters. The primary difference shown in Figure 2.3 is that the fixed platforms are embedded into the seafloor, while the floating platforms utilize mooring systems to keep themselves in place. The specifics of the different platform designs will be covered in more detail in the following sections.

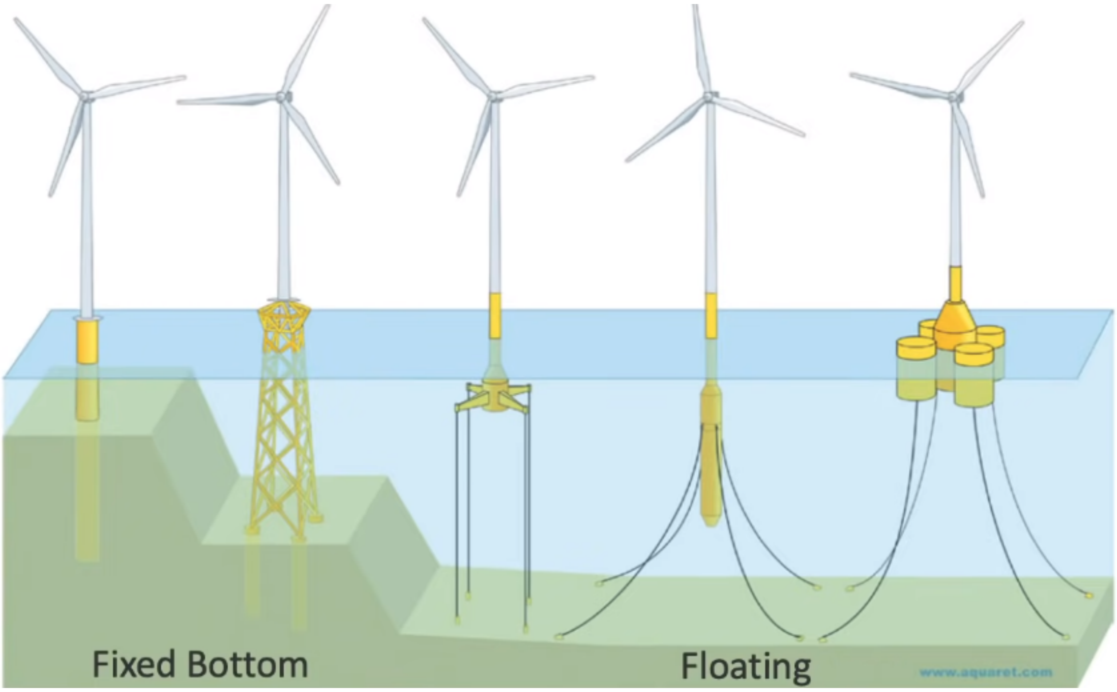

Figure 2.3: Different fixed and floating platform designs, deployed depending on water depths [3]

2.1.1 Fixed-Bottom

The most common fixed bottom wind turbine platform designs are shown in Figure 2.4. Of the six designs presented, the most popular are the monopiles, gravity-base, jacket, and tripod. The monopile foundations is typically 5-6 m in diameter, 50-60 m in lengths, and 500-800 tons in weight [12]. Installation requires hydraulically embedding the foundations into the seabed. These foundations are best suited for water depths ranging from 0-30 m. The gravity-base platform utilizes a concrete structure at its based filled with sand, rock, and iron ore in order to anchor the turbine to the seabed [12]. These foundations are typically best suited for deeper waters, with depths greater than 20 m. The jacket foundation consists of four legs with an interconnected cross structure. These cross braces typically have a diameter of 2 m. Similar to the monopile, the legs of the foundation are driven into the seabed. The jacket foundations are best suited for sites with a water depth between 25 and

50 m [12]. Lastly, the tripod foundation is similar to the jacket design, though only has three legs and does not have the cross braces. The tripod foundation is most feasible in sites with water depth greater than 20 m.

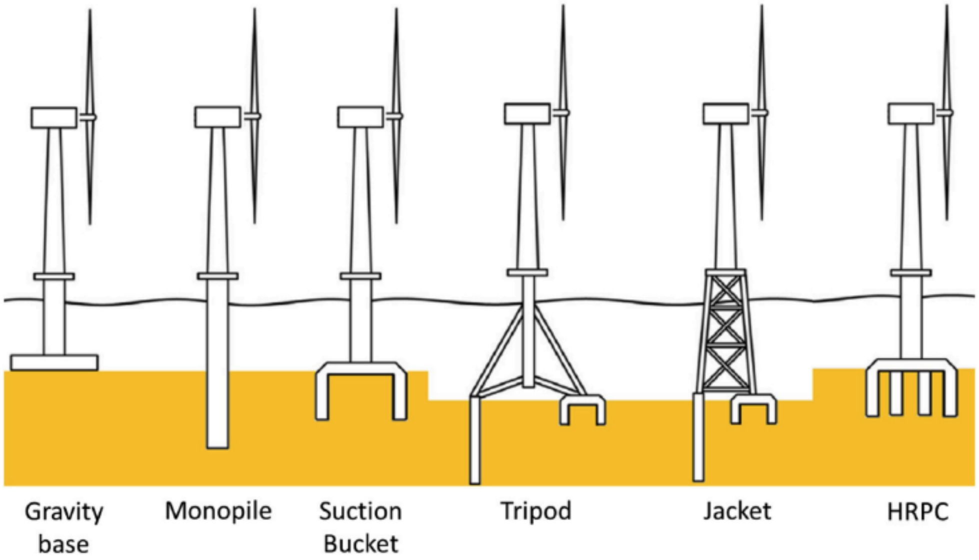

Figure 2.4: Foundation designs for fixed offshore wind turbines

Fixed foundations make up the vast majority of the offshore wind market. Of the 50,623 MW cumulative installed capacity discussed in the previous section, 99.76% is fixed bottom offshore wind [2]. Though in recent years, the trend of wind turbines moving to deeper water is becoming more apparent. Figure 2.5 taken from the 2022 Offshore Wind Market report, shows the depth of different wind farms for each year, including announced farms through 2027. The farms are split between Asian and rest of world projects. The global trend line, in green, shows that over the last three decades, wind farms have been shifting into deeper and deeper water. The trend is even more clear for Asian specific farms, with the blue trend line showing a steep increase in recent years. While this trend towards deeper water could halt at the highest limit of fixed bottom foundations, it is much more likely that the desire to utilize the greater resource further offshore, will push offshore wind towards floating platforms.

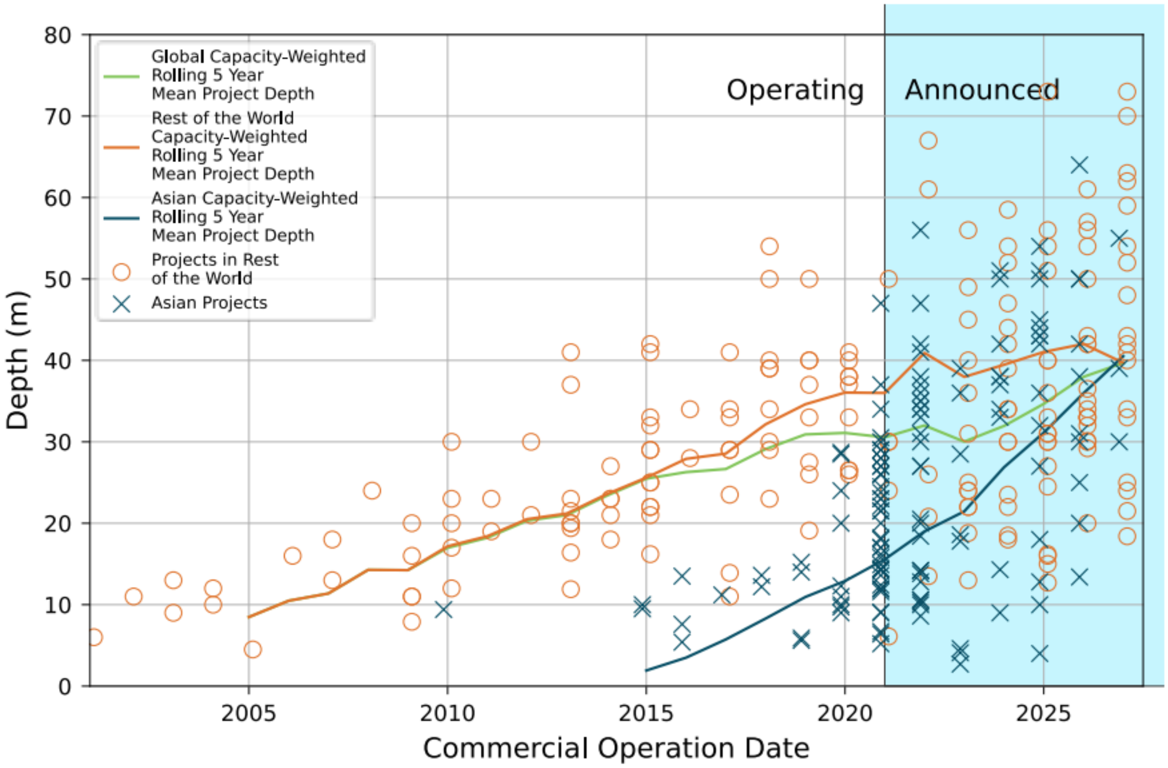

Figure 2.5: Depth of wind farms over the past three decades including projects announced over through 2027 [2]

2.1.2 Floating

The worlds first offshore floating wind farm, Hywind Scotland, was commissioned in 2017 and has a total capacity of 30 MW split between five turbines. In 2021 the worlds largest floating offshore wind farm, Kincardine, located off the coast of Aberdeen, Scotland, was completed. Kincardine includes five, 9.5 MW turbines mounted on semisubmersible platforms [2]. As discussed earlier, the most critical component of these floating turbines is the floating platform where the turbine is mounted. Similar to the fixed-bottom turbines, there exists several different floating platform designs, including the semisubmersible approach used for the Kincardine farm. The main platform designs used for floating wind turbines include the spar, tension leg platforms and semisubmersible. These designs are shown in Figure 2.6 [3].

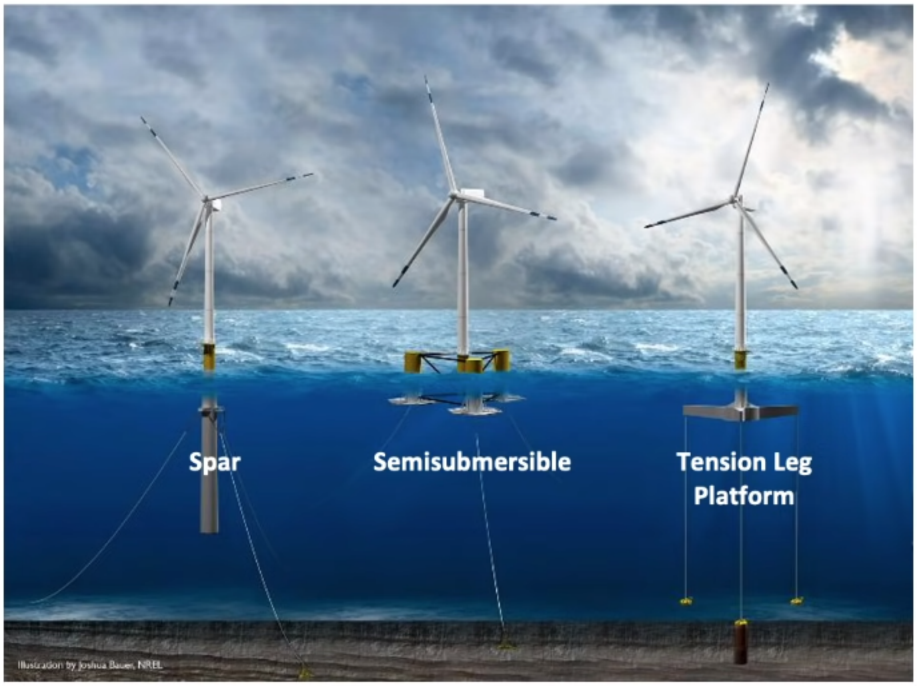

Figure 2.6: Common designs for offshore floating wind platforms [3]

The spar platform design, was originally developed by the company StatoilHydro, in Norway. As part of the Offshore Code Comparison Collaboration, NREL modified this spar concept to be compatible with NREL's 5 MW turbine [13] [14]. The design itself includes a slender, deeply drafted spar buoy [4]. This buoy is moored to the seabed using three catenary mooring lines. The OC3 spar was designed for a water depth of 320 m and includes a total draft of 120 m. As of 2021, spar platforms support 37.9 MW of offshore wind, making it the second most common behind the semisubmersible platform.

The tension leg platform was developed collaboratively between NREL and MIT. A full design and load analysis in an NREL report published back in 2010 [15]. The tension leg platform consists of four legs extending off of a central spar. These legs are each moored to the seabed through taut mooring lines. The bottom of the central spar is weighted to increase stiffness and improve ease at which the platform can be towed. Currently there are no reported tension leg supported farms in the latest market report, though their use is expected to increase over the next five years.

The semisubmersible platform design was originally developed for the University of Maine DeepCwind project. Similar to the spar design, the semisubmersible was later modified,by NREL, such that it is compatible with the with NREL's 5 MW turbine [16]. The design includes three large columns oriented in a triangle, connected to a central column via cross braces. The turbine is mounted on the central columns, and the entire system is moored to the seabed using catenary mooring lines. Traditionally, the three outer columns would be filled with ballast water, however, as discussed in the introduction, this study will analyze the effect of replacing this ballast with TMDs and TIDs for structural control. Currently, semisubmersible platforms support 81.3 MW of offshore floating wind.

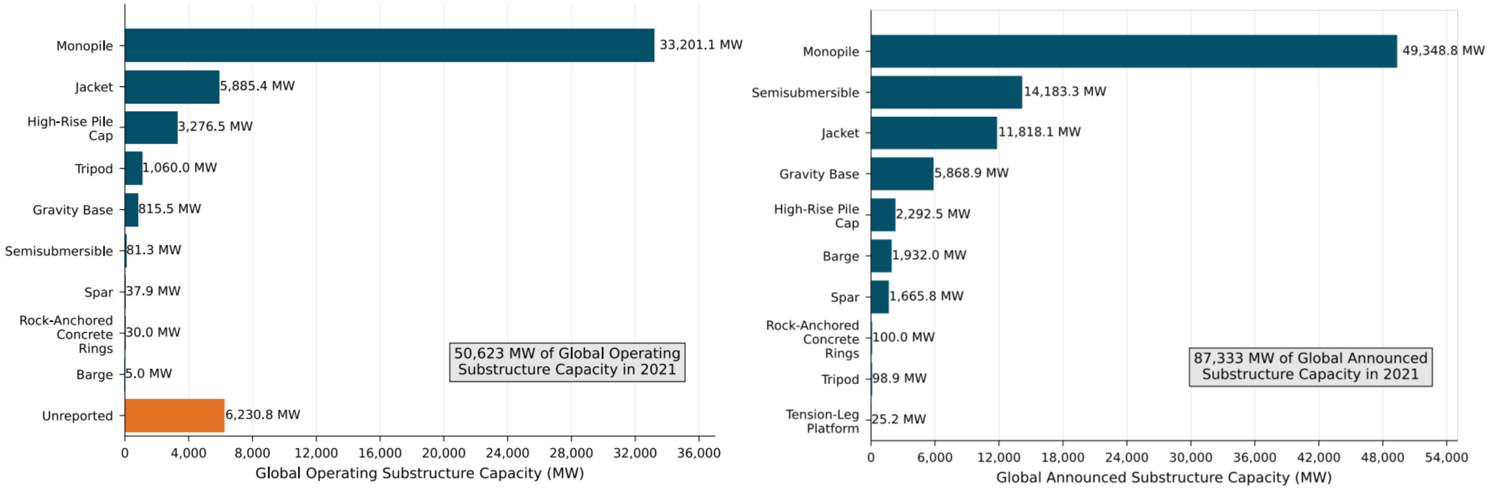

(a) Substructures deployed as of 2021 **(b)** Substructures announced as of 2021

Figure 2.7: Current and future substructure trends for offshore wind [2]

The semisubmersible platform is of interest for this report largely due to its popularity in the offshore floating wind space. Figure 2.7 shows the technology trends for offshore wind, with 2.7a showing the current substructures being used, and 2.7b showing accounting for farms planned as of 2022 [2]. As of 2021, the offshore wind market is still dominated by fixed bottom, with the top five most used substructures being occupied by the most popular fixed bottom designs. Figure 2.7b, shows that the announced wind projects as off 2021 will make the semisubmersible platform one of the most common substructures, second only to the monopile design. That is a jump from 81.3 MW as of 2021, all the way to 14,183 MW supported by semisubmersible platforms. This exponential growth can only be expected to continue as the offshore wind market shifts further and further offshore.

Beyond technological shifts, the offshore floating wind market is projecting significant growth through 2027. Figure 2.8 shows the current state and projected growth of the offshore floating wind market, in terms of cumulative installed capacity [2]. Between 2022 and 2027 the cumulative installed capacity of offshore floating wind is expected to jump from 123 MW to 8,362 MW. This increase its stake in the overall offshore market to 4.7%, up significantly from its current stake of 0.03%. Figure 2.8 also specifies the leading countries in offshore floating wind. The United Kingdom leads the way, with South Korea expected to contribute significantly by 2027.

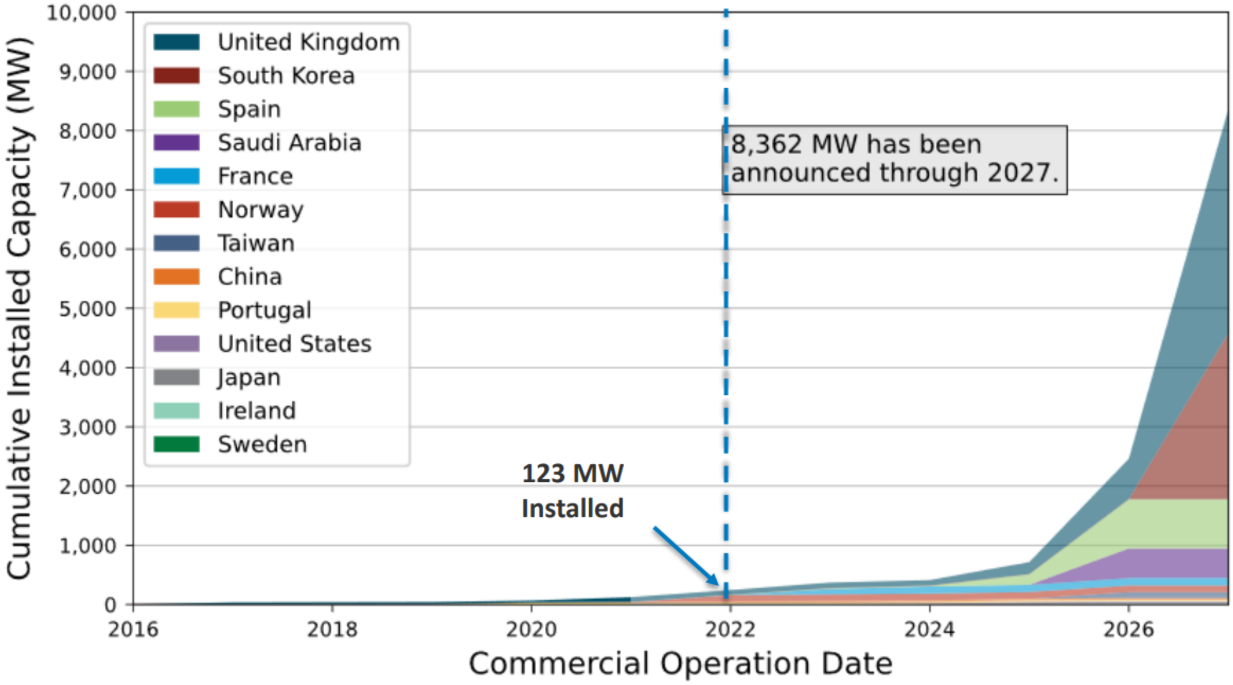

Figure 2.8: Growth of the offshore floating wind market through 2027 [2]

2.1.3 Floating Platform Load Analysis

While it is true that offshore wind is shifting into deeper waters and that floating platforms seem poised to take on a much larger role in the offshore market, studies have shown that the non-fixed nature of these platforms leave them susceptible to higher loads. In a report published by NREL in 2011, a load analysis was conducted for several different offshore floating wind platform concepts [4]. The ultimate loads of the floating platform concepts were determined for multiple loading cases using FAST, an NREL developed tool for modeling wind turbines [17]. In order to better understand the trade-offs between the different floating platform concepts, the ultimate loads were compared to results, under the same design conditions, of land based wind turbines. Figure 2.9 shows the sea-to-land ratios for the ultimate loads of the different floating platform designs [4].

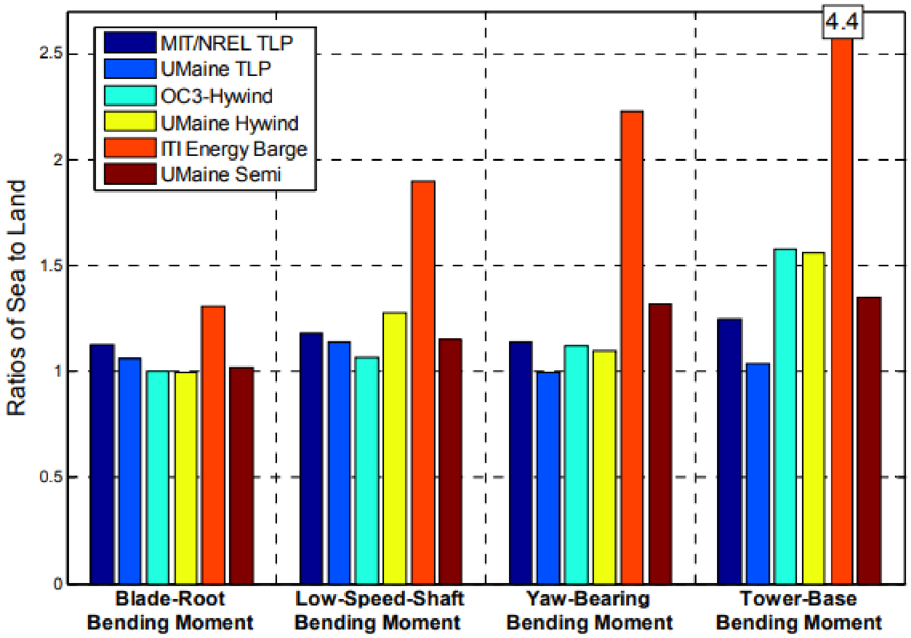

Figure 2.9: Sea to land ratios of ultimate loads for the different floating platform concepts [4]

The ultimate loads are calculated for four different critical bending moments: the blade-root bending moment, the low-sped-shaft bending moment, the yaw-bearing bending moment and the tower-base bending moment. The floating concepts discussed in the previous section include the MIT/NREL tension leg platform, the OC3-Hywind which is equivalent to the spar concept, and the UMaine Semi which is equivalent to the semisubmersible concept. Given that the topic of this study is centered around implementing structural control methods into the semisubmersible platform concept, it is only necessary to analyze the results for the UMaine Semi concept in detail.

It was found that the semisubmersible platform experienced much larger heave motion and smaller pitch motion compared to the spar concepts [4]. This larger heave motion is evidenced by much a much larger ultimate load ratio for the yaw-bearing bending moment, compared to the OC3-Hywind. And the smaller pitching motion shows in the smaller ultimate load ratio for the tower-base bending moment, compared to the OC3-Hywind [4]. Though looking at Figure 2.9, it is clear that the floating platforms as a whole tend to experience larger loads than land based or fixed-bottom wind turbines. For the semisubmersible concept in particular the increased loads are induced largely by excessive heave motion and, to a lesser extent, by pitch motion. Given these results, the goal of this study is to explore whether traditional and non-traditional structural control methods could be implemented into the semisubmersible platform in order to reduce heave and pitch motion.

2.2 Structural Control

Structural control is a field within civil engineering that looks to reduce the dynamic response of buildings through the integration of various subsystems to the larger primary structure. The four main classes of structural control are passive, active, hybrid, and semi-active [18]. The oldest and most studied of these classes is passive control. Passive structural control refers to devices or subsystems that do not require an external power source in order to provide vibration reduction. Given its successful history and relative ease of implementation compared to other structural control methods, passive structural control will main method of focus in this study. More specifically, this study will focus on one of the oldest and most researched forms of passive structural control, the tuned mass damper (TMD).

2.2.1 Tuned Mass Dampers

A TMD is a spring-mass-damper system connected to a primary mass designed for vibration reduction. The reductions comes from tuning the natural frequency of the spring-mass-damper system to the natural frequency of the primary system, thereby canceling out the systems motion at that dominant frequency. A diagram of the most basic TMD is shown in Figure 2.10. The idea for such a vibration damping device was first proposed in a patent in 1911 by Frahm [19]. Since then TMDs have become widely used for reducing wind and earthquake loads in large buildings all across the globe. Perhaps the most famous example of this is the massive, exposed tuned mass damper in the Taipei 101 in Taiwan, shown in Figure 2.11.

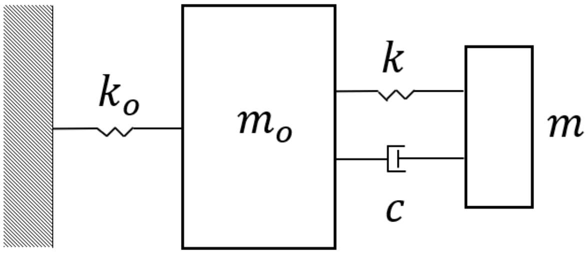

Figure 2.10: Diagram of a simple TMD

TMDs are now commonplace in vibrations textbooks and there exists several reviews highlighting the benefit of adding such devices to structures [20] [21]. Though in recent years it has been found that the functionality and benefit of traditional TMDs can be improved by the addition of a device known as an inerters. The combination of traditional TMDs with these new inerters has given rise to a new class of device used for structural control, commonly referred to as the tuned inerter damper (TID).

Figure 2.11: Image of Taipei 101 in Taiwan and of the pendulum type TMD located within the tower

2.2.2 Tuned Inerter Damper

An inerter is a device similar to a spring and damper in the sense that it is used to connect two bodies. The difference with an inerter is that the force produced by motion of two bodies is proportional to the relative acceleration rather than displacement or velocity. The inerter was first introduced by Smith in 2002, as a novel device with potential uses in fields such as vibration absorption and vehicle suspension [22]. Since then, research into the use of interters for structural control has taken off. With several researchers finding the inerter to be a valuable addition to traditional TMD frameworks [23] [24]. The biggest benefit potential benefit of the TID, is the ability to produce similar amounts of passive control with a fraction of the secondary mass. This is because in one sense, the inerter behaves very similarly to a mass itself, and is able to alleviate the need for such large physical masses in structural control systems. This thought is analyzed in more detail in this study.

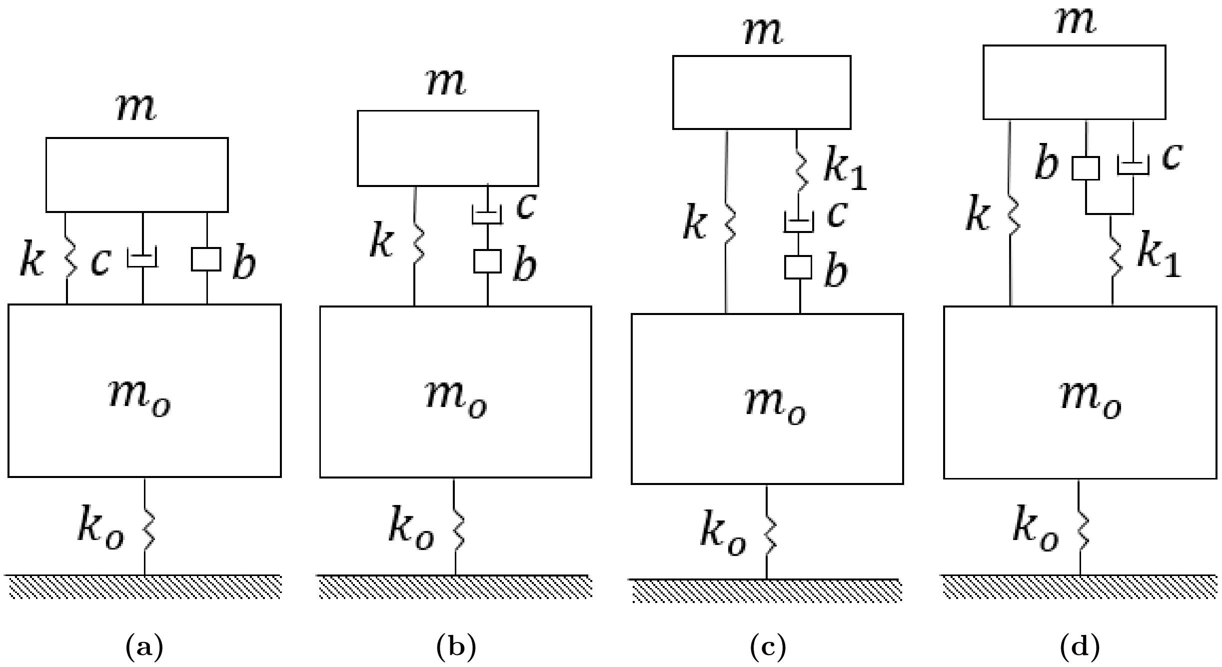

Figure 2.12: Different TID configurations

With the addition of the inerter, the different configurations available for structural control devices increases significantly. The traditional TMD consists of a secondary mass connected to a primary mass by a spring and damper in parallel, but consider how the quality of reduction may change if an inerter is added in parallel. Or perhaps an inerter is added in series with the damper, or an extra spring is added in series with the inerter and damper in parallel. How would this effect the performance of the system? Would it perform better than a traditional TMD system? Is there an optimal configuration? These questions have been addressed in literature, and results showed that inerter based structural control systems consistently outperform traditional TMD systems. Furthermore, one study compared a traditional TMD to several different TID configurations [25]. Some of these configurations are shown in Figure 2.12. Of these configurations, it was found that the configuration shown in Figure 2.12d, consistently outperforms all other configurations in both H_2 and H_∞ optimizations. For this reason, this study will not only analyze the affect of adding traditional TMDs to the semisubmersible platform, but also the affect of adding the optimal TID configuration shown in Figure 2.12d.

2.2.3 Structural Control in Offshore Floating Wind

Before presenting a study concerned with analyzing the affects of adding structural control to floating offshore wind platforms, it is important to first review the research that has already been conducted in this field. That way a clear gap can be defined for the work of this thesis to fill.

Research into the addition of structural control into offshore floating wind increased with the development of a structural control module for FAST, known as FAST-SC [26]. FAST-SC is a modified version of the NREL software FAST mentioned in a previous section. This new module was developed by Dr. Matthew Lackner at the University of Massachusetts Amherst in 2009. The goal was to allow for structural control devices such as TMD's to be implemented into offshore wind turbines and platforms in order to analyze any potential benefit. Dr. Lackner published a study in 2011 that looked to utilize this new module to implement TMD's into the nacelle of a wind turbines supported by a barge-type and monopile support structure [27]. The study concluded that the addition of passive control into the different wind turbines had a uniformly positive impact in the structural response compared to the baseline [27]. Si et al. modeled the effects of adding a TMD into a spar platform that could move in the fore-aft direction [28]. This study found that the TMD was most effective when placed in the upper side of the spar platform, and that for large spring and damping constants the systems saw moderate load reductions [28]. Several models were developed by Stewart with the intention of determining an optimal passive TMD configuration for the monopile, barge, spar, and TLP designs, with the goal of reducing tower fatigue [29]. Results showed that all floating and fixed bottom platforms analyzed in the study saw a reduction in fatigue damage as a result of the passive TMDs.

While the semisubmersible platform design is newly popular in the field, studies still exist analyzing the effects of adding structural control. Li et al. studied the effects of adding a single fore-aft TMD into the nacelle and platform of a semisubmersible supported wind turbine [30]. The study found that a low frequency TMD tuned to the platform pitch natural frequency works well to the vibration of the platform and tower. Moreover, the same TMD configuration was most effective at suppressing regular wave excitation. Han et al. also analyzed the effects fore-aft TMDs, placed in the nacelle and platform, would have on the loading of a semisubmersible supported wind turbine [31]. The results showed that the platform and nacelle TMDs mitigated the influence of the tower fundamental and platform pitch frequencies. Xue et al. researched the effect of adding three tuned liquid multi-column dampers to the semisubmersible platform and found that the system provided reductions to pitch motion by up to 18.53% near the resonance frequency [32].

Studies have also been conducted researching the impact inerters can play on structural control of offshore wind turbines. Hu et al. implemented various, passive inerter based control configurations into the tower of a barge-type floating offshore wind turbine [33]. The configurations analyzed includes the optimal configuration that is discussed in Section 2.2.2 and that is analyzed thoroughly throughout this thesis. Hu et al. showed that the overall performances can be improved using inerters, except for TMD working space, and tower-top fore-aft loading. Sarkar et al. modeled a spar-type floating offshore wind turbine with a tuned mass damper fluid-inerter implemented into the nacelle. Results showed that the inerter based structural control performed significantly better than the traditional TMD [34].

Ma et al. modelled an inerter-based vibration isolation system for heave motion reduction of semisubmersible platforms [35]. The semisubmersible platform modeled in by Ma et al. is a different from the platform discussed in Section 2.1.2, and is more prevalent in oil applications. The study demonstrated that the inerter based control proved more effective than traditional structural control systems.

2.3 Contributions to the State of the Art

Based on the results of the literature review, this thesis will look to research the following gaps regarding structural control applications in the offshore floating wind market.

- An in-depth analysis is conducted studying the effects of implementing a traditional passive TMD system into the three columns of the OC4 semisubmersible platform design. The traditional TMD system is compared to the optimal inerter based control configuration, discussed in Section 2.2.2, and henceforth referred to as the optimal TID configuration. The TMDs and TIDs are oriented within the three columns such that they move vertically in the z-direction. This is a novel configuration that has not yet been explored in literature. In chapter 3 models are derived for the baseline, traditional TMD, and optimal TID configurations. These models are verified using the software WEC-Sim.

- In chapter 4 the results of several parameter optimizations using a pattern search algorithm is presented. The first optimizations looks to reduce the root mean square (RMS) value for heave and pitch free decay responses. A subsequent analysis looks to quantify how much mass can be saved using the optimal TID configuration to achieve the same reduction as the traditional TMD configuration. The final optimization looks to reduce the RMS value for the systems response to regular wave excitation. This regular wave optimization is conducted for a sea state representative of the conditions the system would experience once deployed. Finally, an irregular wave analysis is conducted to see how well a system tuned to a significant wave frequency performs under irregular wave excitation. The overall goal of this analysis is the quantify how effective traditional structural control methods are at reducing the heave and pitch responses of a semisubmersible platform, using a novel TMD configuration. As well as, identifying how the performance of non-traditional, inerter based, structural control methods compares to the traditional TMD method.

Chapter 3

Model Derivations

This chapter begins with a description of the linear potential flow based hydrodynamic forces used to characterize the surrounding fluid. Then the full derivations for the baseline semisubmersible model, the platform with TMDs model, and the platform with optimal TIDs model are presented.

3.1 Hydrodynamics Formulation

For this study, all wave related forces are calculated using linear hydrodynamic coefficients obtained from ANSYS AQWA. AQWA is a frequency-domain potential flow Boundary Element Method (BEM) solver, where BEM solutions are determined by solving the Laplace equation for the velocity potential. The primary assumptions of this method are that the flow is inviscid, incompressible, and irrotational. A more detailed look into the theory behind BEM solvers can be found in the WAMIT user manual [36].

The hydrodynamic forces used in this study include $F_{rad}(t)$, the force and torque resulting from wave radiation, $F_B(t)$, the buoyancy force and torque, and $F_{exc}(t)$, the force and torque caused by incident and diffracted waves. These forces are all functions of the frequency dependent hydrodynamic coefficients acquired from AQWA, highlighted in Table 3.1. Equations 3.1-3.2 show the expressions for $F_{rad}(t)$ and $F_B(t)$.

$$F_{rad}(t) = \begin{bmatrix} A_{11} & A_{13} & A_{15} \\ A_{31} & A_{33} & A_{35} \\ A_{51} & A_{53} & A_{55} \end{bmatrix} * \begin{Bmatrix} \ddot{x}_1 \\ \ddot{x}_3 \\ \ddot{x}_5 \end{Bmatrix} + \begin{bmatrix} C_{11} & C_{13} & C_{15} \\ C_{31} & C_{33} & C_{35} \\ C_{51} & C_{53} & C_{55} \end{bmatrix} * \begin{Bmatrix} \dot{x}_1 \\ \dot{x}_3 \\ \dot{x}_5 \end{Bmatrix} \tag{3.1}$$

$$F_B(t) = \begin{bmatrix} K_{11} & K_{13} & K_{15} \\ K_{31} & K_{33} & K_{35} \\ K_{51} & K_{53} & K_{55} \end{bmatrix} * \begin{Bmatrix} x_1 \\ x_3 \\ x_5 \end{Bmatrix} \tag{3.2}$$

The diagonal terms of the added mass, radiation damping and hydrostatic stiffness matrices are the primary hydrodynamic coefficients, i.e. how motion in that degree of freedom affects the forces in that degree of freedom. While the off diagonal terms create a coupling between the different degrees of freedom, i.e. how motion in one degrees of freedom affects the forces in another degree of freedom. The subscripts 1, 3, and 5, refer to surge, heave and pitch respectively. Also, as indicated in Table 3.1 all hydrodynamic coefficients are function of wave frequency. Therefore, prior to running a simulation, the desired wave frequency must be specified, so that the corresponding hydrodynamic coefficients can be selected. The expression for the regular wave excitation is shown in Equation 3.3.

$$F_{exc,reg}(t) = \frac{H}{2} * \begin{bmatrix} F_{exc,re,1}\cos(\omega t) - F_{exc,im,1}\sin(\omega t) \\ F_{exc,re,3}\cos(\omega t) - F_{exc,im,3}\sin(\omega t) \\ F_{exc,re,5}\cos(\omega t) - F_{exc,im,5}\sin(\omega t) \end{bmatrix} \tag{3.3}$$

Where $F_{exc,re,i}$ and $F_{exc,im,i}$ are the real and imaginary terms of the excitation force coefficient returned by AQWA. Once again, a wave frequency would need to be specified in order to select the correct coefficients. This study also looks to apply irregular wave excitation to the system using a Bretschneider spectrum. The equation for this irregular wave excitation

Table 3.1: Hydrodynamic coefficients returned from the BEM solver AQWA, where ω is the wave frequency

Term	**Description**
$A_{i,j}(\omega)$	Added mass for the 'i' degree of freedom, as influenced by the 'j' degree of freedom
$C_{i,j}(\omega)$	Radiation damping for the 'i' degree of freedom, as influenced by the 'j' degree of freedom
$K_{i,j}(\omega)$	Hydrostatic stiffness for the 'i' degree of freedom, as influenced by the 'j' degree of freedom
$F_{exc,i}(\omega)$	Sum of the Froude-Krylov and diffraction coefficients for the 'i' degree of freedom. Contains real and imaginary terms i.e. $F_{exc,i}(\omega) = F_{exc,re,i}(\omega) + iF_{exc,im,i}(\omega)$

is shown in Equation 3.4,

$$F_{exc,irreg}(t) = \sum_{j=1}^{N} \sqrt{2S(\omega_j)d\omega} \begin{bmatrix} F_{exc,re,1}\cos(\omega_j t + \phi) - F_{exc,im,1}\sin(\omega_j t + \phi) \\ F_{exc,re,3}\cos(\omega_j t + \phi) - F_{exc,im,3}\sin(\omega_j t + \phi) \\ F_{exc,re,5}\cos(\omega_j t + \phi) - F_{exc,im,5}\sin(\omega_j t + \phi) \end{bmatrix} \tag{3.4}$$

where ϕ is a vector of random phase angles the same length as the time vector t, ω_j is the jth term in the wave spectrum used to define the irregular sea state, $d\omega$ is the step size used for the wave spectrum, and $S(\omega_j)$ is the Bretschneider spectrum value for the frequency value ω_j. The Bretschneider spectrum is defined by Equation 3.5,

$$S(\omega) = \frac{5}{16} * \frac{\omega_{sig}^4}{\omega^5} * h_{sig} * exp(-1.25 * \frac{\omega_{sig}^4}{\omega^4}) \tag{3.5}$$

where ω_{sig} is the significant wave frequency, h_{sig} is the significant wave height, and ω is the vector of frequencies used to define the spectrum.

Free decay tests will only involve the buoyancy and radiation forces, while any regular and irregular wave studies also include the wave excitation force from Equation 3.3 and 3.4, respectively. For the free decay and irregular wave cases, the hydrodynamic coefficients are still determined using a single significant wave frequency common in areas where the system will be deployed. This simplification will be discussed in more detail in a later section. For more information on linear wave theory, and the hydrodynamic formulation used in this study, the WEC-Sim theory manual is a good resource [37].

3.2 Baseline Model

A diagram of the 3 DOF baseline model is shown in Figure 3.1. Where the DOFs are platform surge, heave, and pitch or $x_1(t)$, $z_1(t)$ and $\theta_1(t)$ respectively. Two of these DOF are used to define the global vector, $\vec{r}_1$, defined by Equation 3.6. This global vector is the same across all three models presented in this study.

$$\vec{r}_1 = \begin{bmatrix} x_1(t) \\ z_1(t) \end{bmatrix} \tag{3.6}$$

The only properties relevant for the baseline model are the platform mass m_1 and the platform inertia J_1. Given the simplicity of the baseline model, it is possible to provide the equations of motion in Equation 3.7, for the TMD and optimal TID models this will not be the case. For free decay tests, only $F_{rad}(t)$ and $F_B(t)$ are used, though when running regular wave tests, $F_{exc}(t)$ must also be included.

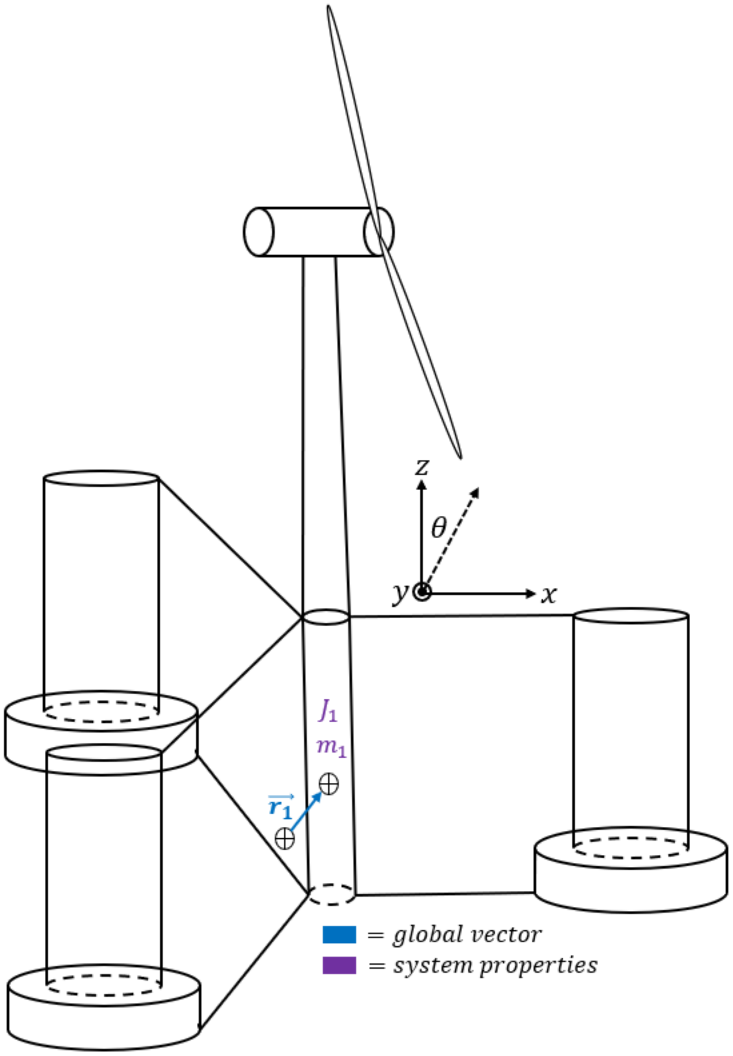

Figure 3.1: Diagram of the baseline semisubmersible platform

$$\begin{bmatrix} m_1 & 0 & 0 \\ 0 & m_1 & 0 \\ 0 & 0 & J_1 \end{bmatrix} * \begin{Bmatrix} x_1(t) \\ z_1(t) \\ \theta_1(t) \end{Bmatrix} = -F_{rad}(t) - F_B(t) + F_{exc}(t) \tag{3.7}$$

3.3 Tuned Mass Damper Model

A diagram of the 6 DOF TMD model can be seen in Figure 3.2. This diagram includes labels for all relevant global vectors, body fixed vectors, variable vectors, and system properties. Descriptions of all system properties can be found in Table 3.2, while the 6 degrees of freedom are outlined in Table 3.3.

Table 3.2: New system properties relevant to the TMD model

Term	Description
$m_2,\ m_3,\ m_4$	Tuned mass within column A, B, and C respectively
$J_2,\ J_3,\ J_4$	Inertia of the tuned mass within column A, B, and C respectively
$k_2,\ k_3,\ k_4$	Stiffness connecting the tuned mass to the top of column A, B, and C respectively
$c_2,\ c_3,\ c_4$	Damping connecting the tuned mass to the top of column A, B, and C respectively
L_x	'x' distance between the CG of the platform and the top of columns A and C
L_z	'z' distance between the CG of the platform and the top of columns A and C

The equations of motion for this multi-body 6 DOF system are determined using the energy method or as it is also called, the Lagrangian method [38]. This method makes use of the Euler-Lagrange equation, Equation 3.8.

$$\frac{d}{dt}\frac{\partial L}{\partial \dot{q}_i} - \frac{\partial L}{\partial q_i} + \frac{\partial R}{\partial \dot{q}_i} = 0 \tag{3.8}$$

Where,

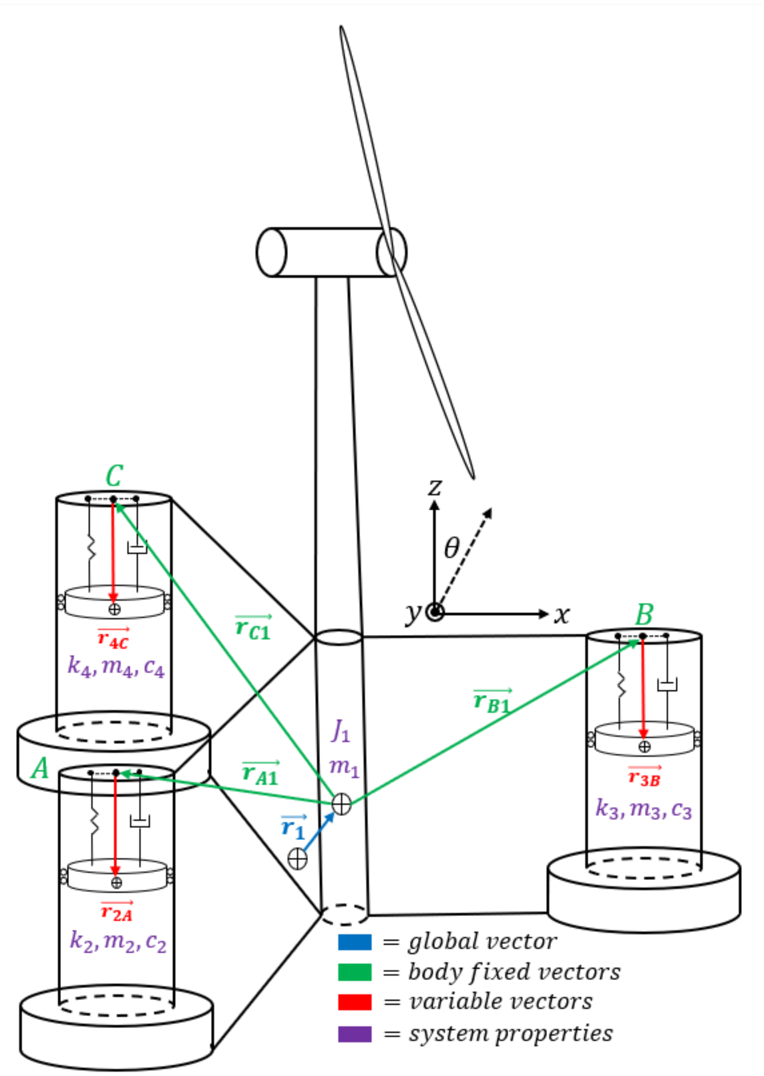

Figure 3.2: Diagram of the semisubmersible platform with TMDs

$$L = T - U \tag{3.9}$$

is an expression termed the Lagrangian. And T, U, and R are the system's kinetic energy, potential energy, and Rayleigh dissipation function respectively. While q_i and $\dot{q}_i$ represent the 'ith' degree of freedom and its corresponding velocity. The Euler-Lagrange equation is carried out an 'i' number of times, resulting in an equation of motion for each degree of freedom. Prior to using the Euler-Lagrange equation one must first develop the expressions for T,

Table 3.3: DOF for the TMD model

Term	Description
$x_1(t)$	Surge motion of the platform
$z_1(t)$	Heave motion of the platform
$\theta_1(t)$	Pitch motion of the platform
$L_2(t)$	Scalar distance between the tuned mass in column A and the top of column A
$L_3(t)$	Scalar distance between the tuned mass in column B and the top of column B
$L_4(t)$	Scalar distance between the tuned mass in column C and the top of column C

U, and R. These expressions will inherently be functions of the DOFs, making the eventual partial derivatives of Euler-Lagrange equation possible. For this model, the standard $[x, z]$ coordinate of the tuned masses is ignored, instead relative distances between the tuned masses and the columns are defined, see Table 3.3. Therefore, prior to writing an expression for the kinetic energy, the positions and velocities of the masses must first be written in terms of these new relative distances. This is accomplished using body fixed vectors that move and rotate with the platform, as well as variable vectors that not only move and rotate with the platform, but also track the location of the mass in their respective column. These variable vectors are functions of the relative distances, $L_2(t)$, $L_3(t)$, and $L_4(t)$, introduced earlier. Both the body fixed and variable vectors are defined on Figure 3.2. Expressions for the body fixed vectors are shown in equations 3.10-3.12

$$\vec{r}_{A1} = \begin{bmatrix} -L_x \\ L_z \end{bmatrix} \quad (3.10) \qquad \vec{r}_{B1} = \begin{bmatrix} 2L_x \\ L_z \end{bmatrix} \quad (3.11) \qquad \vec{r}_{C1} = \begin{bmatrix} -L_x \\ L_z \end{bmatrix} \quad (3.12)$$

The notation for these vectors indicates the two points they are connecting, for example $\vec{r}_{A1}$ defines a vector connecting the CG of body 1 (the platform) to the top of column A. The two lengths used to form these body fixed vectors are defined in Table 3.2. Also, consider that because these are 2-D planar models, i.e. only tracking motion and rotation occurring within the xz-plane, the body fixed vectors defining the location of the top of column A and C are identical. Expressions for the variable vectors are shown in equations 3.13-3.15.

$$\vec{r}_{2A} = L_2(t)\hat{u} \quad (3.13) \qquad \vec{r}_{3B} = L_3(t)\hat{u} \quad (3.14) \qquad \vec{r}_{4C} = L_4(t)\hat{u} \quad (3.15)$$

Where $\hat{u}$ is a unit vector defining the current orientation of the tuned mass with respect to the platform, for this study $\hat{u}$ is defined as:

$$\hat{u} = \begin{bmatrix} 0 \\ -1 \end{bmatrix} \tag{3.16}$$

indicating that the mass is directly below the top of the column. This serves as the initial position of the masses and is rotated over time as the platform pitches. The rotations of the body fixed and variable vectors are carried out using a 2-D rotation matrix defined by Equation 3.17.

$$R = \begin{bmatrix} \cos(\theta_1(t)) & -\sin(\theta_1(t)) \\ \sin(\theta_1(t)) & \cos(\theta_1(t)) \end{bmatrix} \tag{3.17}$$

Combining the concepts of global vectors, body fixed vectors, variable vectors, and rotation matrices, it is now possible to define the global position of the masses as a function of the relative distances introduced earlier. The positions of the masses over time are defined by equations 3.18-3.20.

$$\vec{r}_2 = \begin{bmatrix} x_2 \\ z_2 \end{bmatrix} = \vec{r}_1 + R * \vec{r}_{A1} + R * \vec{r}_{2A} = \begin{bmatrix} x_1 - L_x \cos(\theta_1) - L_z \sin(\theta_1) + L_2 \sin(\theta_1) \\ z_1 - L_x \sin(\theta_1) + L_z \cos(\theta_1) - L_2 \cos(\theta_1) \end{bmatrix} \tag{3.18}$$

$$\vec{r}_2 = \begin{bmatrix} x_2 \\ z_2 \end{bmatrix} = \vec{r}_3 + R * \vec{r}_{B1} + R * \vec{r}_{3B} = \begin{bmatrix} x_1 + 2L_x \cos(\theta_1) - L_z \sin(\theta_1) + L_3 \sin(\theta_1) \\ z_1 + 2L_x \sin(\theta_1) + L_z \cos(\theta_1) - L_3 \cos(\theta_1) \end{bmatrix} \tag{3.19}$$

$$\vec{r}_4 = \begin{bmatrix} x_4 \\ z_4 \end{bmatrix} = \vec{r}_1 + R * \vec{r}_{C1} + R * \vec{r}_{4C} = \begin{bmatrix} x_1 - L_x \cos(\theta_1) - L_z \sin(\theta_1) + L_4 \sin(\theta_1) \\ z_1 - L_x \sin(\theta_1) + L_z \cos(\theta_1) - L_4 \cos(\theta_1) \end{bmatrix} \tag{3.20}$$

The velocities of the masses over time, are found by simply taking the time derivative of equations 3.18-3.20. These velocities are defined by equations 3.21-3.23.

$$\vec{v}_2 = \begin{bmatrix} \dot{x}_2 \\ \dot{z}_2 \end{bmatrix} = \begin{bmatrix} \dot{x}_1 + L_x \sin(\theta_1)\dot{\theta}_1 - L_z \cos(\theta_1)\dot{\theta}_1 + \dot{L}_2 \sin(\theta_1) + L_2 \cos(\theta_1)\dot{\theta}_1 \\ \dot{z}_1 - L_x \cos(\theta_1)\dot{\theta}_1 - L_z \sin(\theta_1)\dot{\theta}_1 - \dot{L}_2 \cos(\theta_1) + L_2 \sin(\theta_1)\dot{\theta}_1 \end{bmatrix} \tag{3.21}$$

$$\vec{v}_3 = \begin{bmatrix} \dot{x}_3 \\ \dot{z}_3 \end{bmatrix} = \begin{bmatrix} \dot{x}_1 - 2L_x \sin(\theta_1)\dot{\theta}_1 - L_z \cos(\theta_1)\dot{\theta}_1 - \dot{L}_3 \sin(\theta_1) - L_2 \cos(\theta_1)\dot{\theta}_1 \\ \dot{z}_1 + 2L_x \cos(\theta_1)\dot{\theta}_1 - L_z \sin(\theta_1)\dot{\theta}_1 - \dot{L}_3 \cos(\theta_1) + L_3 \sin(\theta_1)\dot{\theta}_1 \end{bmatrix} \tag{3.22}$$

$$\vec{v}_4 = \begin{bmatrix} \dot{x}_4 \\ \dot{z}_4 \end{bmatrix} = \begin{bmatrix} \dot{x}_1 + L_x \sin(\theta_1)\dot{\theta}_1 - L_z \cos(\theta_1)\dot{\theta}_1 + \dot{L}_4 \sin(\theta_1) + L_4 \cos(\theta_1)\dot{\theta}_1 \\ \dot{z}_1 - L_x \cos(\theta_1)\dot{\theta}_1 - L_z \sin(\theta_1)\dot{\theta}_1 - \dot{L}_4 \cos(\theta_1) + L_4 \sin(\theta_1)\dot{\theta}_1 \end{bmatrix} \tag{3.23}$$

With these expressions for the velocities of the masses over time, as a function of the relative distances between the tops of the columns, it is now possible to define the kinetic energy of the system. The kinetic energy, potential energy, and dissipation function for the TMD model are defined by equations 3.24-3.26

$$\begin{aligned} T =& \frac{1}{2}m_1\dot{x}_1^2 + \frac{1}{2}m_1\dot{z}_1^2 + \frac{1}{2}(J_1 + J_2 + J_3 + J_4)\dot{\theta}_1^2 + \\ & \frac{1}{2}m_2\dot{x}_2^2 + \frac{1}{2}m_2\dot{z}_2^2 + \frac{1}{2}m_3\dot{x}_3^2 + \frac{1}{2}m_3\dot{z}_3^2 + \frac{1}{2}m_4\dot{x}_4^2 + \frac{1}{2}m_4\dot{z}_4^2 \end{aligned} \tag{3.24}$$

$$U = \frac{1}{2}k_2(L_{2,0} - L_2)^2 + \frac{1}{2}k_3(L_{3,0} - L_3)^2 + \frac{1}{2}k_4(L_{4,0} - L_4)^2 \tag{3.25}$$

$$R = \frac{1}{2}c_2\dot{L}_2^2 + \frac{1}{2}c_3\dot{L}_3^2 + \frac{1}{2}c_4\dot{L}_4^2 \tag{3.26}$$

This model is completed by carrying out the Euler-Lagrange equation, using equations 3.24-3.26, for each degree of freedom and then formatting the resulting equations of motion such that they can be solved using a differential equation solver. For the TMD and optimal TID model, the Euler-Lagrange equation is carried out symbolically and formatted using MATLAB.

3.4 Optimal Tuned Inerter Damper Model

A diagram of the platform plus optimal tuned inerter damper model is shown in Figure 3.3. The main difference between the TMD and TID models is that the traditional damper is replaced by the optimal TID configuration. This optimal configuration includes a damper and inerter in parallel, connected to the mass by a spring in series. The additional spring in series introduces a new intermediate point in each column. Three new relative distances are defined from these intermediate points to the tops of the columns. These relative distances along with all other degrees of freedom for the optimal TID model are defined in Table 3.5. Moreover, all new or modified system properties for the optimal TID model can be seen in Table 3.4.

The definitions for the body fixed vectors, equations 3.10-3.12, and variable vectors, equations 3.13-3.15, from the TMD model, remain the same for this derivation. However, the new relative distances required three new variable vectors, defined by equations 3.27-3.29.

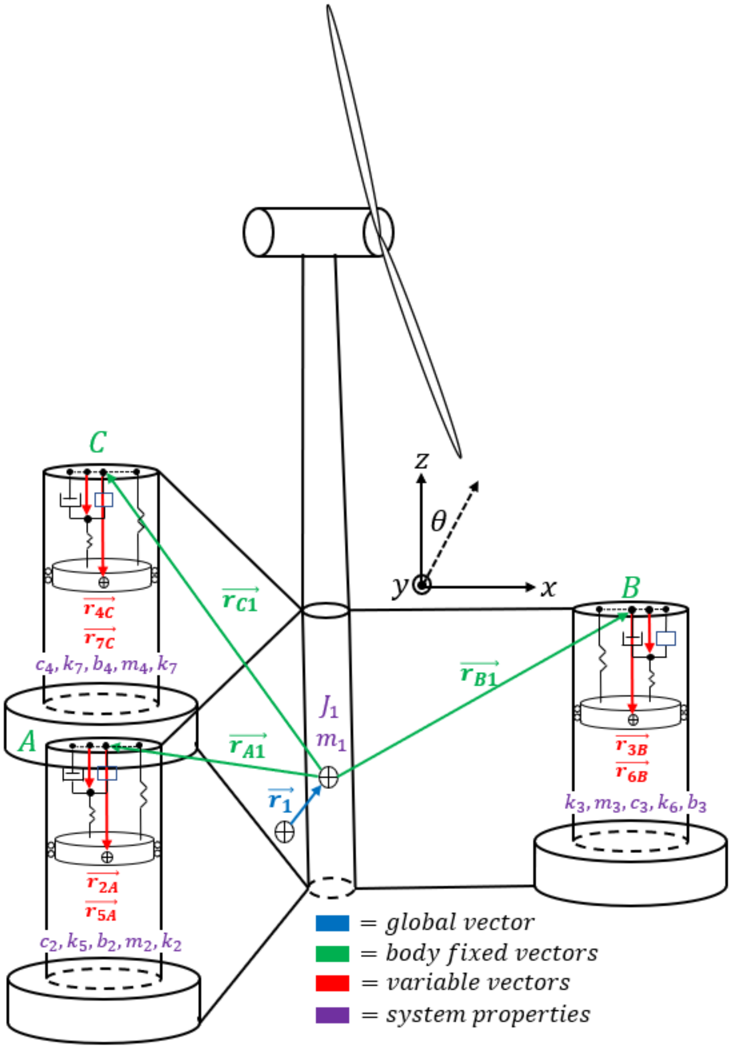

Figure 3.3: Diagram of the semisubmersible platform with the optimal TIDs

$$\vec{r}_{5A} = L_5(t)\hat{u} \quad (3.27) \qquad \vec{r}_{6B} = L_6(t)\hat{u} \quad (3.28) \qquad \vec{r}_{7C} = L_7(t)\hat{u} \quad (3.29)$$

The new intermediate points are considered to have zero mass. As a result, their position has no impact on the kinetic energy, meaning it is not necessary to define the positions and velocities of these points as was done for the masses in the previous section. This new model can simply use these same expressions for the velocities of the masses, equations 3.18-3.20. While the effects of the optimal TID configuration appear in the new expressions for the kinetic energy, potential energy, and dissipation function, defined by equations 3.30-3.32.

Table 3.4: New or modified system properties relevant to the optimal TID model

Term	**Description**
$k_2,\ k_3,\ k_4$	Stiffness connecting the tuned mass to the top of column A, B, and C respectively
$k_5,\ k_6,\ k_7$	Stiffness connecting the tuned mass to intermediate point of column A, B, and C respectively
$c_2,\ c_3,\ c_4$	Damping connecting the intermediate point to the top of column A, B, and C respectively
$b_2,\ b_3,\ b_4$	Inertance connecting the intermediate point to the top of column A, B, and C respectively

$$\begin{aligned}T =&\frac{1}{2}m_1\dot{x}_1^2 + \frac{1}{2}m_1\dot{z}_1^2 + \frac{1}{2}(J_1 + J_2 + J_3 + J_4)\dot{\theta}_1^2 +\\ &\frac{1}{2}m_2\dot{x}_2^2 + \frac{1}{2}m_2\dot{z}_2^2 + \frac{1}{2}m_3\dot{x}_3^2 + \frac{1}{2}m_3\dot{z}_3^2 + \frac{1}{2}m_4\dot{x}_4^2 + \frac{1}{2}m_4\dot{z}_4^2 +\\ &\frac{1}{2}b_2\dot{L}_5^2 + \frac{1}{2}b_3\dot{L}_6^2 + \frac{1}{2}b_4\dot{L}_7^2\end{aligned} \tag{3.30}$$

$$\begin{aligned}U =&\frac{1}{2}k_2(L_{2,0} - L_2)^2 + \frac{1}{2}k_3(L_{3,0} - L_3)^2 + \frac{1}{2}k_4(L_{4,0} - L_4)^2 +\\ &\frac{1}{2}k_5((L_{2,0} - L_{5,0}) - (L_2 - L_5))^2 + \frac{1}{2}k_6((L_{3,0} - L_{6,0}) - (L_3 - L_6))^2 +\\ &\frac{1}{2}k_7((L_{4,0} - L_{7,0}) - (L_4 - L_7))^2\end{aligned} \tag{3.31}$$

$$R = \frac{1}{2}c_2\dot{L}_5^2 + \frac{1}{2}c_3\dot{L}_6^2 + \frac{1}{2}c_4\dot{L}_7^2 \tag{3.32}$$

The inerters add three new terms to the expression for kinetic energy, while the additional springs add three new terms to the kinetic energy. Consider that since these new springs are between the intermediate point and the masses, it is necessary to find the difference between the two relative distances defined for each column. Lastly, given the new location of the dampers within the column, the relative distances between the top of the column and the intermediate points must be used. Similar to the TMD model, the actual equations of motion for the optimal TID model are found by carrying out the Euler-Lagrange model symbolically in Matlab for each degree of freedom. This process will be discussed in more detail in the following section.

3.5 Model Verification

The primary method used for verifying the models derived in this study is using WEC-Sim [39]. WEC-Sim is an open-source modeling tool developed by the National Renewable Energy Laboratory and Sandia National Laboratory for modeling fluid structure interactions using linear potential flow theory. Given that the models used in this study utilize the same method for modeling hydrodynamics, it makes WEC-Sim an ideal tool for verification. With that being said, WEC-Sim, does not currently have the functionality for modeling the optimal TID configuration within the platform. In other words, WEC-Sim's current library does not allow for the addition of an inerter as a connection block, focusing more on the traditional spring and damper connection. For this reason, only the baseline and TMD models are verified using this method. However, given that the optimal TID model is just an extension of the TMD model, with identical hydrodynamics, verification of the TMD model

Table 3.5: DOFs for the TID model

Term	**Description**
$x_1(t)$	Surge motion of the platform
$z_1(t)$	Heave motion of the platform
$\theta_1(t)$	Pitch motion of the platform
$L_2(t)$	Scalar distance between the tuned mass in column A and the top of column A
$L_3(t)$	Scalar distance between the tuned mass in column B and the top of column B
$L_4(t)$	Scalar distance between the tuned mass in column C and the top of column C
$L_5(t)$	Scalar distance between the intermediate point in column A and the top of column A
$L_6(t)$	Scalar distance between the intermediate point in column B and the top of column B
$L_7(t)$	Scalar distance between the intermediate point in column C and the top of column C

is considered sufficient for this study.

3.5.1 WEC-Sim Verification Setup

WEC-Sim's primary use is for modeling wave energy converters (WECs), though it can model the fluid structure interactions for any geometry as long as the necessary BEM data is provided. The verification is completed by running two nearly identical free decay tests and one regular wave case using both WEC-Sim and the derived models and plotting the results. The free decay tests include a heave decay test with a one meter drop, and a pitch decay test with a five degree initial rotation. The regular wave case is for a 3 meter wave with a 6 second wave period. A visualization of the pitch free decay test is shown in Figure 3.4. In general, this figure provides a great view of how the tuned masses move within the platform to reduce vibration.

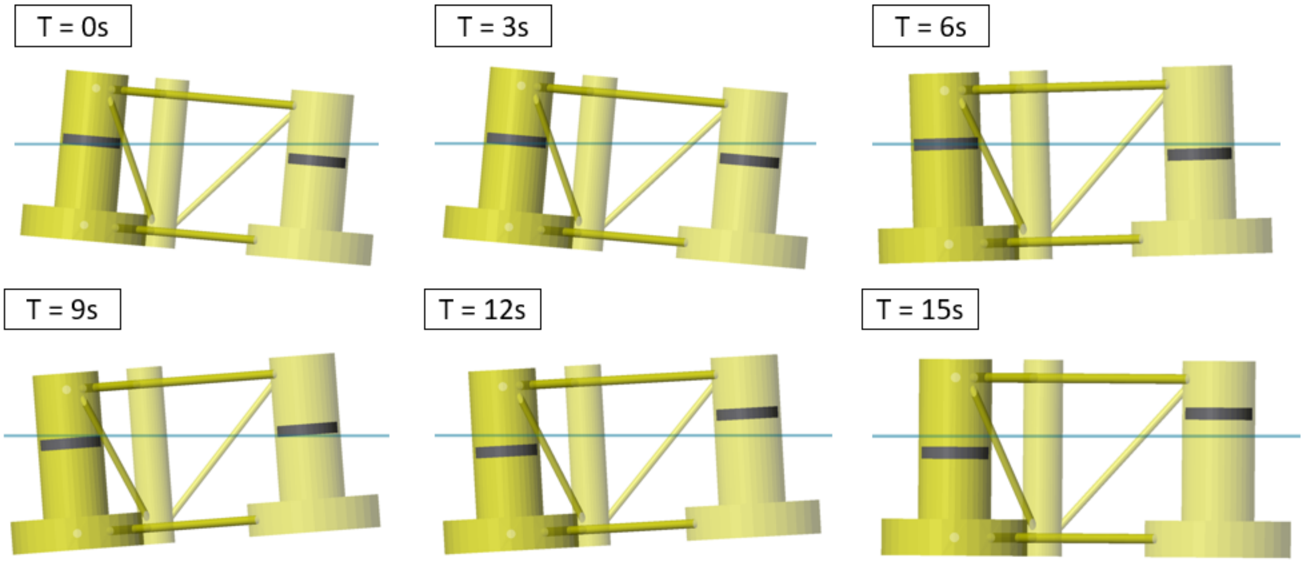

Figure 3.4: Snapshots of the WEC-Sim TMD model used to verify the TMD model

The properties used for the verification free decay tests are shown in Table 3.6. For this verification, the goal was to model a system as close as possible to the full scale semisubmersible floating platform defined in the NREL technical report "Definition of the Semisubmersible Floating System for Phase II of OC4" [16]. The values for platform inertia (J_1) and platform specific lengths ($L_x \, and \, L_z$) are taken directly from that technical report. Moreover, the geometry files used as inputs for the BEM solvers were modeled after the specifications provided by the technical report. The value for the mass comes directly from the BEM data, given that WEC-Sim directly determines the mass of the floating body from the displaced volume provided by the BEM files. If any other mass value is used then the system will not settle at the desired water line. This also explains why the total mass of the tuned masses is subtracted from the platform mass for the verification study. If not, then the free decay tests would settle below the desired water line. This total mass value is still very similar to the value provided in the technical report for the platform, given that a nearly identical platform geometry was used for determining the BEM data. The parameters for the tuned mass, stiffness and damping are considered to be uniform across the columns. The tuned masses roughly correspond to a 5% mass ratio, while the stiffness and damping values are on the same order of magnitude as expected optimal values. The initial distances between the tuned masses and top of the platform ($L_{2,0}$, $L_{3,0}$, *and* $L_{4,0}$,) are also uniform between the columns and are chosen such that the masses rest directly in the middle of the columns. Lastly, a wave period of 6 seconds is chosen for determining the hydrodynamic coefficients used for the simulation. This wave period is very common at offshore sites in the Atlantic where such a system might be deployed. For the regular wave verification all of the same property values are used from Table 3.6 except the stiffness and damping of the TMDs. A stiffness of 280,000 N/m and damping of 100 Ns/m are chosen for the regular wave verification in order to create a response unique compared to the baseline.

Table 3.6: Property values used for free decay verification

Property	**Value**	**Property**	**Value**
m_1 (kg)	13,831,300 - 3m	L_x (m)	14.435
J_1 $(kg - m^2)$	6.827e9	L_z (m)	25.46
$J_{2,3,4}$ $(kg - m^2)$	1,500,000	$L_{2,0}$ (m)	13.00
$m_{2,3,4}$ (kg)	250,000	$L_{3,0}$ (m)	13.00
$k_{2,3,4}$ (N/m)	50,000	$L_{4,0}$ (m)	13.00
$c_{2,3,4}$ (Ns/m)	50,000	T (s)	6

To clarify, for the verification of the derived models, heave and pitch free decay tests are conducted for the baseline and TMD configurations. A regular wave case is also simulated for both configurations. The tests are run using both WEC-Sim and the derived model and results are compared in the following section. The system properties used in the verification are representative of only the platform, given the WEC-Sim condition discussed earlier. For the optimization runs presented later, the system properties are representative of a complete turbine system and are derived in Section 3.6.

3.5.2 Free Decay Verification Results

The results for the verification of the baseline configuration can be seen in Figure 3.5. This figure includes the results of the heave free decay test comparison, Figure 3.5a, and pitch free decay test comparison, Figure 3.5b. The black line represents the WEC-Sim model, while the dashed blue line shows the derived model. Visually, it is clear that the results line up almost exactly for both decay tests, though a comparison of root mean square (RMS) values is also presented in Table 3.7. The baseline columns for both the heave and pitch free decay test show that the WEC-Sim and derived models have the same RMS value.

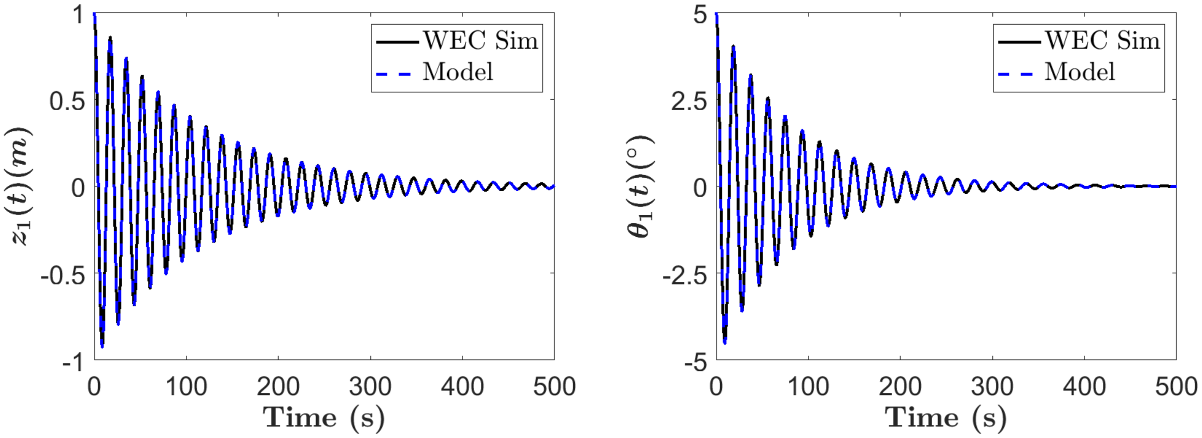

(a) Heave free decay **(b)** Pitch free decay

Figure 3.5: Free decay test comparison between WEC-Sim and the derived model for the **baseline** configuration

The results for the verification of the TMD configuration are shown in Figure 3.6. Curves showing the relative distance between column A and the corresponding tuned mass, $L_2(t)$, are included for further comparison between the two modeling methods. Similar to the baseline case, visually the curves seem to line up with each other perfectly. The TMD model columns in Table 3.7, shows that the RMS values for the heave decay test are exactly the same. The values for the pitch decay test are nearly the same, showing only a 2% difference between the two methods. This difference is likely due to a rounding error with the inertia's used for models, or due to how the WEC-Sim model handles pretension for a pitching system. Regardless, this 2% difference is considered acceptable for this verification.

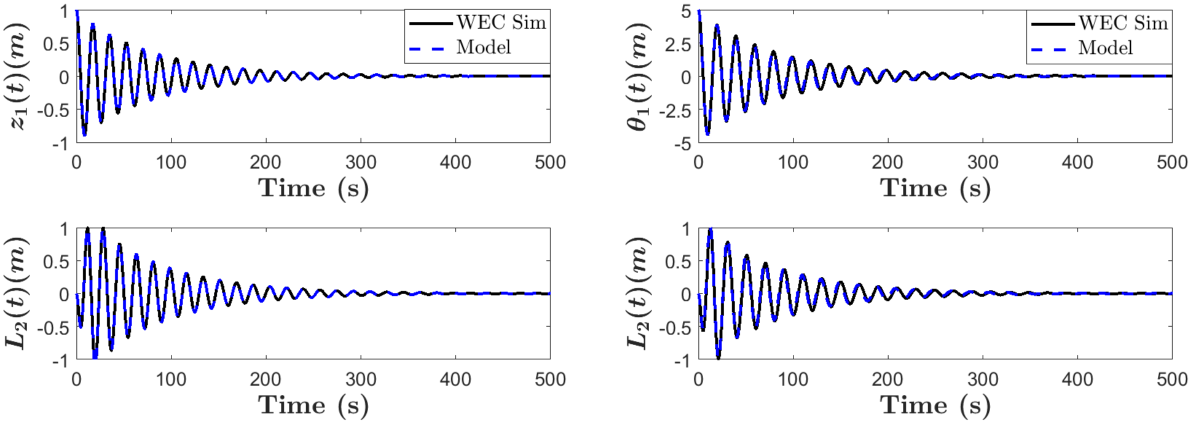

(a) Heave free decay **(b)** Pitch free decay

Figure 3.6: Free decay test comparison between WEC-Sim and the derived model for the **TMD** configuration

The verification tests conducted for this study included comparison between the derived models and WEC-Sim for two different free decay tests. These heave and pitch free decay tests were conducted for both the baseline model and the TMD model. The properties used were representative of a platform only system, with property values drawn from an NREL technical report introducing the semisubmersible platform concept [16]. Verification results showed near perfect agreement in RMS values between the two different configuration for both free decay tests, with the pitch decay test for the TMD configuration showing only a 2% difference between the two models.

Table 3.7: Results of the free decay test verification for both the baseline and TMD configurations

Verification Results							
Heave Free Decay RMS Values (m)				Pitch Free Decay RMS Values (°)			
Baseline		TMD Model		Baseline		TMD Model	
WEC-Sim	Derived	WEC-Sim	Derived	WEC-Sim	Derived	WEC-Sim	Derived
0.239	0.239	0.197	0.197	1.025	1.025	0.980	1.000

3.5.3 Regular Wave Verification Results

Figure 3.7 shows the heave and pitch responses for both the baseline and TMD configuration. The heave and pitch response of the baseline configuration for the regular wave verification case is shown in Figure 3.7a and 3.7b respectively. Visually, the baseline responses show the WEC-Sim and derived models lining up almost perfectly. This is confirmed by the RMS values presented in Table 3.8. The baseline RMS values for heave and pitch only vary by roughly one ten-thousandth for between the WEC-Sim and derived models.

The heave response of the TMD configuration for the two models are shown in Figure 3.7c. The responses appear to line up very well, and this is further evidenced by the corresponding RMS values in Table 3.8. Once again, the RMS values are only off by roughly one ten-thousandth. Figure 3.7d shows the pitch response of the TMD configuration for both models. Visually, the responses of the two models seem to line up well, though perhaps not as well as the other cases. This slight discrepancy is quantified in Table 3.8, where the RMS values between the two models for varies by roughly three thousandths. A similar discrepancy was seen for the same case in the free decay optimization and the explanation likely remains the same. The slight difference is probably due to a rounding error with the inertias used for models, or due to how the WEC-Sim model handles pretension for a pitching system. Regardless of the slight difference, this regular wave verification has further shown the two

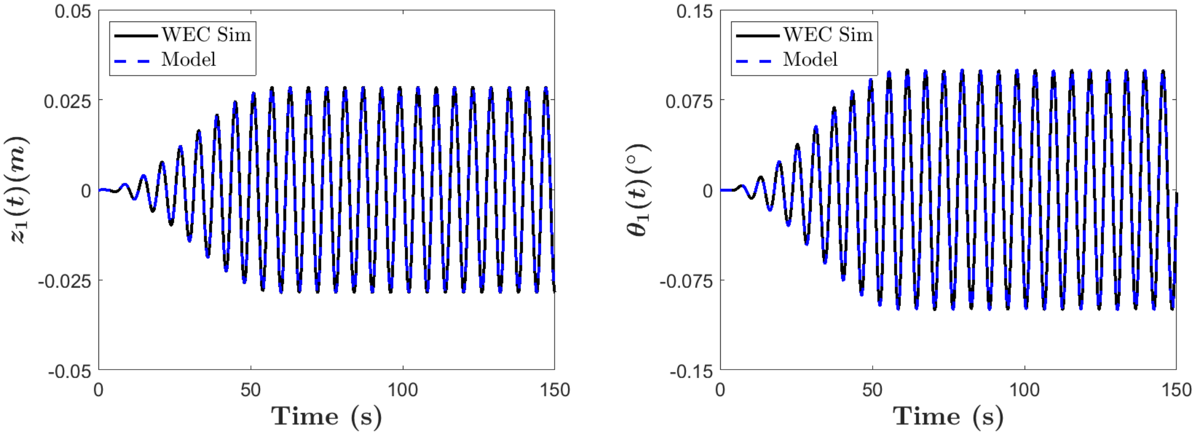

(a) Heave response - baseline **(b)** Pitch response - baseline

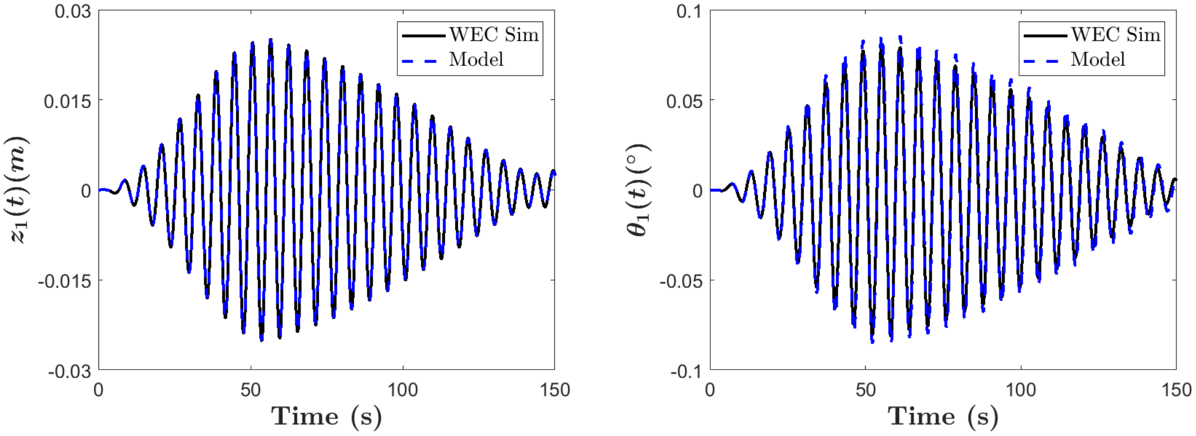

(c) Heave response - TMD **(d)** Pitch response - TMD

Figure 3.7: Regular wave case comparison between WEC-Sim and the derived model for the baseline and TMD configurations

models to be virtually identical.

These results serve as verification for both the TMD and optimal TID models. Future results are derived from integrating these verified models with optimization techniques that will be discussed in Chapter 4. Prior to discussing the optimization and results, mass and inertia values must be derived for a complete platform plus wind turbine system. This derivation is presented in the following section.

Table 3.8: Results of the regular wave verification for both the baseline and TMD configurations

Verification Results							
Heave Response RMS Values (m)				Pitch Response RMS Values (°)			
Baseline		TMD Model		Baseline		TMD Model	
WEC-Sim	Derived	WEC-Sim	Derived	WEC-Sim	Derived	WEC-Sim	Derived
0.0175	0.0174	0.0111	0.0110	0.0609	0.0610	0.0367	0.0394

3.6 Overall System Properties

Before conducting the optimizations, it is necessary to determine the overall and mass, CG, and inertia for a platform plus wind turbine system. All masses, CGs, and inertias of the sub-components are taken from two NREL technical reports [16] [14]. Robertson's, "definition of a semisubmersible floating system" report [16], discussed in the verification section, is used to determine the system properties for the platform and tower. While Jonkman's, "definition of a 5MW reference wind turbine" report, is used to determine the system properties for the nacelle and rotor. The necessary system properties of the sub-components and overall system are presented in Table 3.9, while a diagram showing the locations of the relevant CGs is shown in Figure 3.8. The CG values are z-values with respect to the SWL, x and y CG values are considered to be zero for this study. The overall CG for the system is calculated using Equation 3.33.

$$CG_{Overall} = \sum_{i=1}^{N} \frac{m_i * CG_i}{m_i} \tag{3.33}$$

Where the subscript "i" indicates a certain sub-component and "N" is the total number of sub-components, four in this case. The inertia values for the sub-components are with respect to the axis of rotation located at the overall CG. Platform and tower inertia values

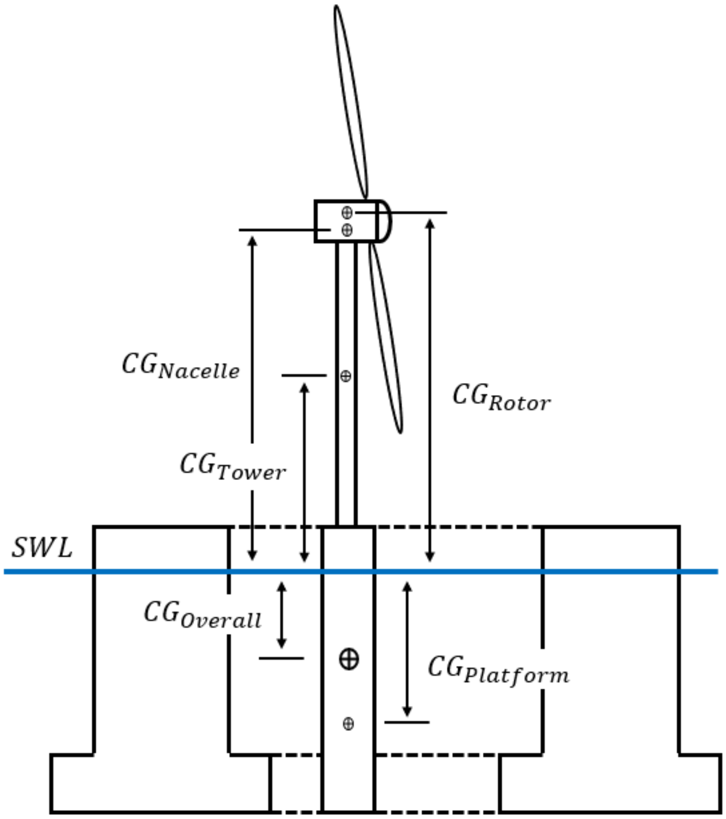

Figure 3.8: 2-D Diagram of the platform plus wind turbine system with labels for all relevant centers of gravity

are obtained using the parallel axis theorem, for example:

$$I_{Tower} = I_{Tower,CG} + m_{Tower}R^2 \tag{3.34}$$

where, $I_{Tower,CG}$ is the inertia of the tower with respect to its own CG and R is the distance from the towers CG to the overall CG. Both of these values can be found in the technical report mentioned earlier. The rotor and nacelle are considered to be point masses, given their relatively small inertias with respect to their own CGs. Therefore, the inertia is simply equal to:

$$I = mR^2 \tag{3.35}$$

for both of those components. The overall inertia is simply the sum of all sub-component inertias. These overall mass and inertia values are used for future optimization and provide a simplified yet accurate representation of the complete platform plus wind turbine system.

Table 3.9: System properties for the complete platform plus wind turbine system. CG values are with respect z-values with respect to the SWL and inertia values of sub-components are with respect to the overall CG

Overall System Properties					
	Platform	Tower	Nacelle	Rotor	Overall
Mass (kg)	1.3473E+07	249,780	240,000	110,000	1.407E+07
CG (m)	-13.46	43.4	89.35	90	-9.89
Inertia ($kg - m^2$)	7.067E+09	8.347E+08	2.364E+09	1.098E+09	1.136E+10

Chapter 4

Parameter Optimization

4.1 Optimization Overview

The optimizations in this study are conducted using the ”pattern search” algorithm within MATLAB’s global optimization toolbox. Several different optimizations algorithms were tested for this study, however, the ”pattern search” algorithm was ultimately selected based on its ability to consistently settle on the global minimum value of the objective function. In short an optimization algorithm seeks to explore a defined design space by varying design parameters and tracking the resulting change in objective function. Surfaces showing this design space i.e., objective function vs. design parameters, for the TMD free decay optimizations are presented in Figure 4.1.

Figure 4.2 shows the actual evolution of the objective function during the course of a heave free decay optimization run. Effectively this plot shows how the optimization algorithm starts at a point near the top of the surface shown in Figure 4.1a and gradually moves that point closer and closer to the global minimum by varying the stiffness and damping values. Utilizing this optimization method, it is possible to determine what stiffness, damping, and inertance values result in the greatest reduction in the objective function value value of a free decay response for any given mass ratio.

The objective functions for heave and pitch free decay tests are introduced in equations 4.1

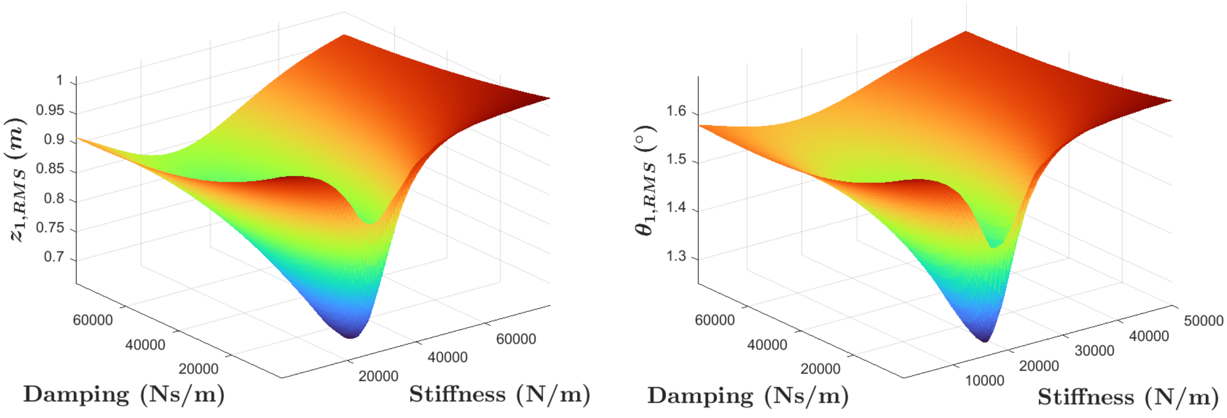

(a) Heave free decay surface

(b) Pitch free decay surface

Figure 4.1: Surfaces showing the objective function of the free decay optimizations as a function of the design parameters

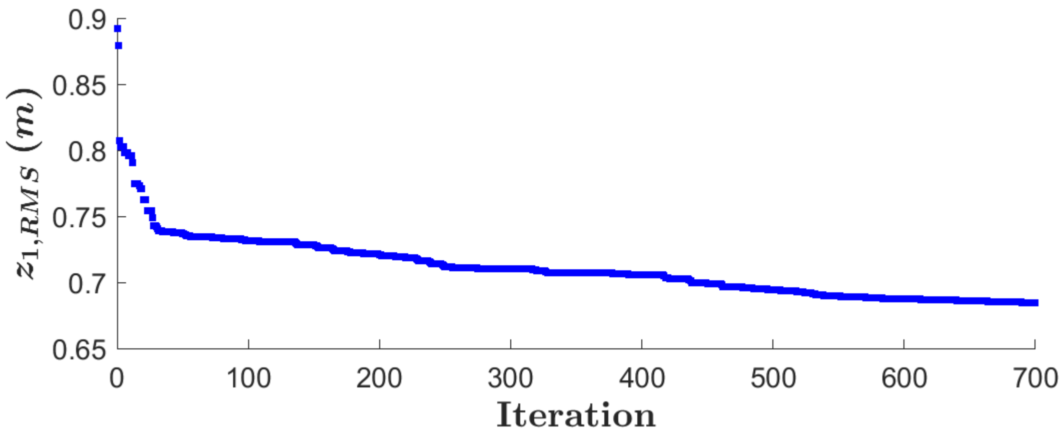

Figure 4.2: Objective function across all iterations of a particular optimization run

and 4.2 respectively. Where the objective functions, $z_{1,RMS}$ and $\theta_{1,RMS}$ are the root mean square of the systems heave and pitch free decay response respectively. Equation 4.1 also serves as the objective function for the regular wave optimization and will be discussed in more detail in Section 4.3.1.

$$\begin{aligned} &TMD: \ Minimize\ z_{1,RMS}(k_{2,3,4}, c_{2,3,4}) \\ &TID: \ Minimize\ z_{1,RMS}(k_{2,3,4}, c_{2,3,4}, k_{5,6,7}, b_{2,3,4}) \end{aligned} \tag{4.1}$$

$$\begin{aligned} &TMD: \ Minimize\ \theta_{1,RMS}(k_{2,3,4}, c_{2,3,4}) \\ &TID: \ Minimize\ \theta_{1,RMS}(k_{2,3,4}, c_{2,3,4}, k_{5,6,7}, b_{2,3,4}) \end{aligned} \tag{4.2}$$

The design parameters for the TMD configuration are simply the stiffness and damping values of the TMDs. While the design parameters for the optimal TID configuration also includes the additional stiffness and inertance values. The RMS values for the objective functions are calculated using Equation 4.3.

$$\theta_{1,RMS} = \sqrt{\frac{1}{N}\sum_{i=0}^{N}\theta_1(\Delta t * i)^2} \tag{4.3}$$

Where θ_1 is the systems pitch position at each time step, $\Delta t * i$. For the optimization, the simulations are run for 250 seconds with a time step of 0.01 seconds. This results in an N value equal to 25,000. Figure 4.3, serves as a visualization of the objective function, showing the RMS value of a baseline and control case for a pitch free decay test. The baseline response is shown in black, with the RMS value specified by the dashed black line. While the control response and RMS value is shown in blue. The goal of the optimization is to lower that horizontal RMS line as much as possible by varying the different design parameters of the control configurations. The RMS value was chosen given that it is not only an effective way to quantify rate at which the system settles, but is also able to be quickly calculated as an objective function within MATLAB. Other values such as decay rate would be more difficult to calculate and pass to an objective function. While Figure 4.3 shows the objective functions for a free decay response, the principle remains the same for a regular wave response.

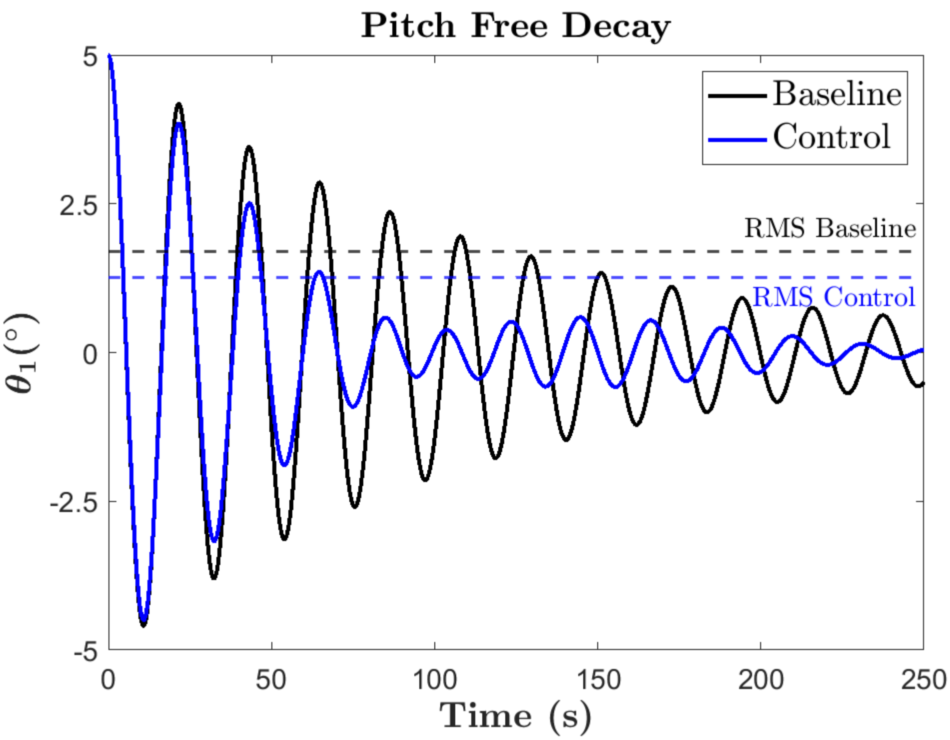

Figure 4.3: Generic pitch free decay responses for the baseline and TMD configuration with RMS values identified by horizontal lines

4.2 Free Decay Optimization

4.2.1 Free Decay Optimization Setup

All system properties used for the free decay and regular wave optimizations are presented in Table 4.1. These properties include the overall mass and inertia derived in Section 3.6, inertia of the tuned masses, distances L_x and L_z with respect to the overall CG. As well as the initial distances from the tuned masses and intermediate points to the tops of the columns.

Table 4.1: Property values used for model optimization

System Properties			
Property	**Value**	**Property**	**Value**
m_1 (kg)	1.407e7	$L_{2,0}$ (m)	13.00
J_1 $(kg - m^2)$	1.136e10	$L_{3,0}$ (m)	13.00
$J_{2,3,4}$ $(kg - m^2)$	1.5e6	$L_{4,0}$ (m)	13.00
L_x (m)	14.435	$L_{5,0}$ (m)	6.50
L_z (m)	21.89	$L_{6,0}$ (m)	6.50
		$L_{7,0}$ (m)	6.50

The free decay optimizations are conducted for a range of different mass ratios, μ. The mass ratio is used to determine $m_{2,3,4}$ for both the TMD and TID configurations. Mass ratios are commonly used for structural control related analysis as it provides a way to tie the secondary mass to the primary mass. This calculation is shown in Equation 4.4

$$m_{2,3,4} = \frac{\mu * m_1}{3} \tag{4.4}$$

The value is divided by three since there are three tuned masses in total. For each mass ratio, the free decay optimizations are conducted and the following values are recorded: optimal parameters and optimal RMS values. Using these optimal RMS values, the percent reduction from the baseline RMS value is calculated using Equation 4.5.

$$\%\ Reduction = \frac{RMS_{Baseline} - RMS_{Control}}{RMS_{Baseline}} * 100 \tag{4.5}$$

Where $RMS_{Baseline}$ is the RMS value calculated from the free decay response of the baseline configuration. And $RMS_{Control}$ is the RMS value calculated from the free decay response of either the TMD or optimal TID configurations. These percent reduction values are plotted at each mass ratio, so that further conclusions can be drawn regarding the trends of the data. Curves are also fit to the data so that the performance of both control methods be more accurately analyzed. The fit equations are used to determine what mass ratios for the optimal TID configuration result in a percent reduction equivalent to the TMD configuration. This analysis is done for each mass ratio i.e., what lower mass ratio for the optimal TID configuration produces the same reduction as the TMD configuration using a 1% mass ratio? 2%? 3%? etc. Ultimately, these different mass ratios are compared to determine how much less mass is required by the optimal TID configuration in order to produce the same reduction as the TMD configuration. This is calculated using Equation 4.6.

$$\Delta Mass = (\mu_{TMD} - \mu_{TID}) * m_1 \tag{4.6}$$

4.2.2 Free Decay Optimization Results

Plots of the optimized heave and pitch free decay responses of the platform for a 5% mass ratio are shown in Figure 4.4, where Figure 4.4a and Figure 4.4b show the optimized heave and pitch response, respectively. This figure visually shows the benefit of adding structural control, with the TMD and optimal TID responses settling much faster than the baseline. Figure 4.4 also shows the optimal TID configuration settling faster than the TMD configuration for both decay tests. Using Matlab's fast Fourier transform function, it is also possible to view the results in the frequency domain. In other words, from the time domain response, it is possible to determine the amplitude of the systems response for a range of frequencies. Figures 4.5a and 4.5b show the frequency domain response for the heave and pitch free decay tests, respectively. Similar to the time domain response plots, these plots also show the control outperforming the baseline and the TID outperforming the TMD. Moreover, the frequency domain plots show natural frequencies that match what is expected from literature. As discussed in the previous section, for this study, these optimal responses are determined for a range of different mass ratios. The resulting RMS values are analyzed using several different methods in order to determine the extent of how beneficial structural control can be to an offshore floating wind system. And whether or not the optimal TID configuration provides substantial benefit over a traditional TMD method of control.

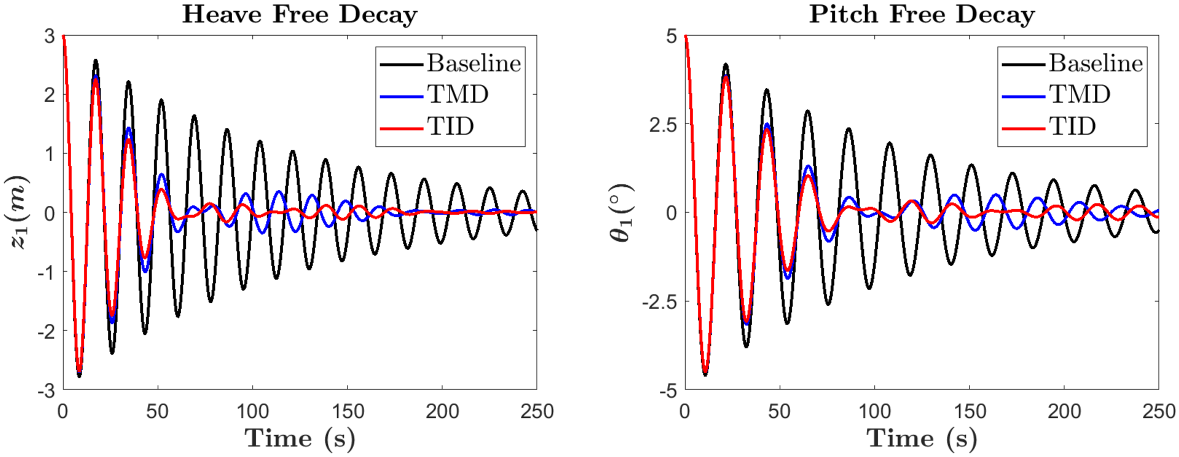

(a) Heave free decay **(b)** Pitch free decay

Figure 4.4: Optimized free decay time domain response for the overall system with a mass ratio of 5%

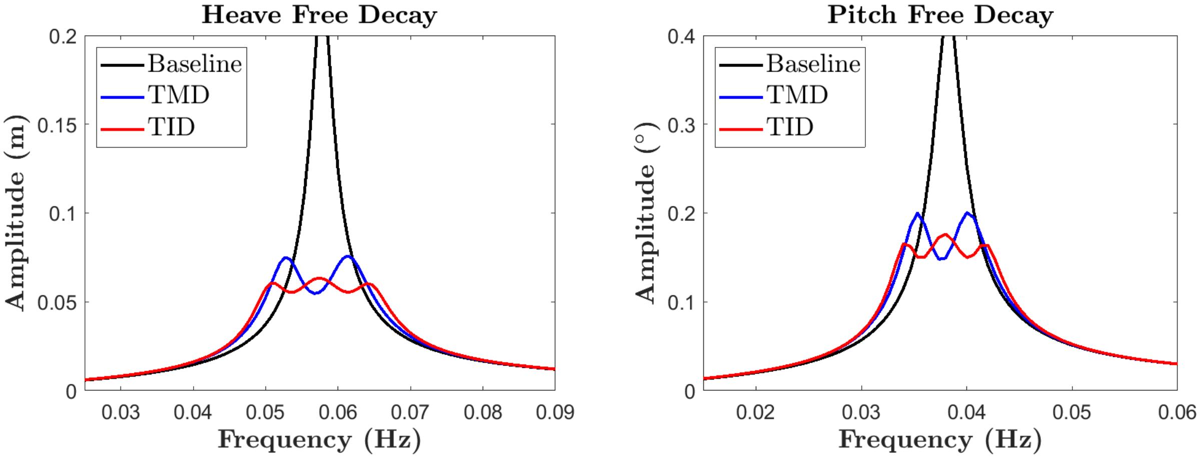

(a) Heave free decay **(b)** Pitch free decay

Figure 4.5: Optimized free decay frequency domain response for the overall system with a mass ratio of 5%

The results of the heave and pitch free decay optimizations are shown in Table 4.2. This table includes the RMS values for the baseline, TMD, and optimal TID configurations for all mass ratios. The table also includes the percent reduction between the baseline and control configurations for all mass ratios. The mass ratios used for this study ranged from 1% to 8% with a step size of 1%. The optimal parameter values that achieved these results can be found in the Appendix.

Table 4.2: Results of the heave and pitch free decay optimizations for baseline and control configurations

Free Decay Optimization Results								
	Heave Free Decay				Pitch Free Decay			
	Platform + TMD		Platform + TID		Platform + TMD		Platform + TID	
μ	RMS (m)	% Reduction	RMS	% Reduction	RMS (°)	% Reduction	RMS	% Reduction
Baseline	1.008	-	1.008	-	1.694	-	1.694	-
0.01	0.817	18.92%	0.801	20.18%	1.471	13.17%	1.459	13.96%
0.02	0.754	25.22%	0.728	27.88%	1.388	18.07%	1.356	19.95%
0.03	0.713	29.29%	0.686	32.51%	1.330	21.53%	1.291	23.82%
0.04	0.683	32.24%	0.655	35.79%	1.284	24.22%	1.242	26.68%
0.05	0.660	34.55%	0.631	38.36%	1.247	26.41%	1.204	28.94%
0.06	0.641	36.43%	0.612	40.45%	1.216	28.25%	1.172	30.84%
0.07	0.625	38.02%	0.596	42.22%	1.189	29.82%	1.144	32.46%
0.08	0.611	39.38%	0.582	43.77%	1.166	31.19%	1.121	33.86%

Focusing on the percent reduction, Table 4.2 shows that both control configurations provide a significant reduction to $RMS_{Baseline}$, for both free decay tests. With the lowest percent reduction in heave and pitch for either configuration still coming out to 18.92% and 13.17% respectively. Table 4.2 also shows that for both configurations and degrees of freedom, increasing the mass ratio results in a significant increase in percent reduction. For example, the percent reductions at mass ratios of 1% and 8% for the heave decay test are 18.92% and 39.38% respectively. That is nearly a +20% increase in reduction for only a +7% increase in mass ratio. Though perhaps the biggest takeaway from Table 4.2 is that the optimal TID configuration outperforms the TMD configuration for both decay tests and all mass ratios. The extent to which the optimal TID outperforms the TMD varies depending on mass ratio, with the largest performance gains occurring at the larger mass ratios. For example, the difference in percent reduction in heave RMS for mass ratios of 1% and 8% are 1.26% and 4.49% respectively. The relationship between percent reduction and mass ratio is further explored in Figure 4.6, where a curve fitting analysis is conducted using the data in Table 4.2.

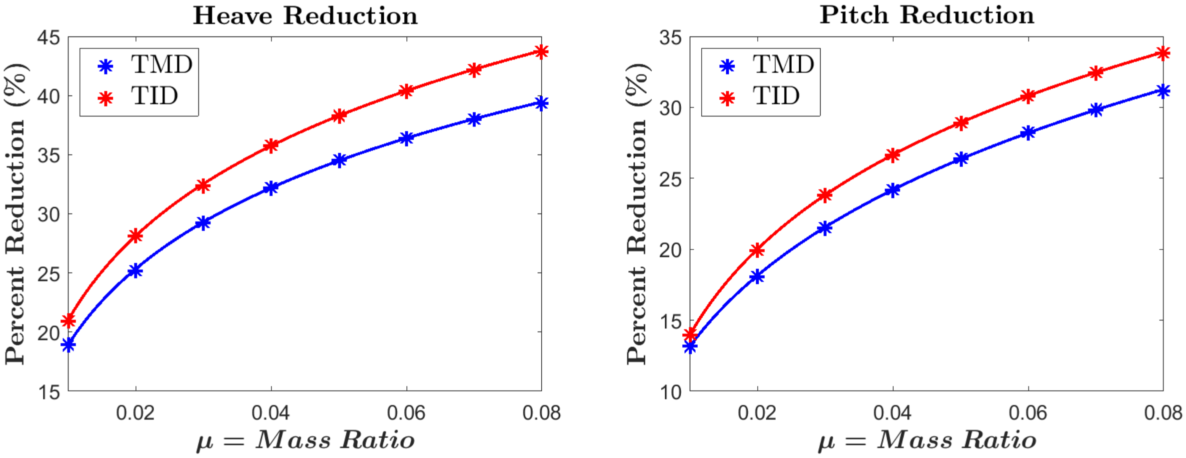

(a) Heave free decay

(b) Pitch free decay

Figure 4.6: Percent reduction vs. mass ratio for both heave and pitch free decay optimization studies

Figure 4.6 shows the percent reduction as a function of mass ratio for both configurations. Where Figure 4.6a and 4.6b show the results for the heave and pitch free decay optimizations respectively. Curves are fit to the data points using the logarithmic fit shown in Equation 4.7.

$$f = a + b * log(x) + c * log(x)^2 \tag{4.7}$$

The values for the curve fitting coefficients and corresponding R^2 values are presented in

Table 4.3 . Figure 4.6 further highlights the points introduced in the previous section i.e., the optimal TID configuration outperforms the TMD configuration, and the performance gap increases as you increase the mass ratio. The figure also shows that the relationship between percent reduction and the mass ratio is logarithmic, with rate of increase starting off relatively large then tapering off to a more constant value. Another interesting takeaway is that the overall percent reduction and gap in performance between the TMD and optimal TID configurations is smaller for the pitch degree of freedom. This is to be expected given that the control subsystems are better oriented for heave reduction. With the masses most naturally able to track with the translational movement of the platform.

Table 4.3: Curve fitting coefficients and R^2 values for the curves in Figure 4.6

Curve Fitting Results				
	a	b	c	R^2
TMD-Heave	69.37	12.92	0.434	0.999
TID-Heave	69.35	10.83	0.050	1.000
TMD-Pitch	65.78	16.38	1.074	0.999
TID-Pitch	64.86	13.71	0.572	1.000

Using the curve fitting information presented in Equation 4.7 and Figure 4.3, it is now possible analyze what mass ratios for the optimal TID configuration would produce the same percent reduction as the TMD configuration. That way it can be determined how much less mass is required by the optimal TID configuration to produce the same benefit. The results of this analysis are presented in Table 4.4. Where Δ *mass* is calculated using Equation 4.6, presented in the previous section. This table further shows that for each mass ratio the optimal TID outperforms TMD configuration. Even at the lowest mass ratio, the optimal TID reduces the overall mass within the columns by 26,170 kg based on the heave optimization and 12,522 kg based on the pitch optimization. The results of the mass reduction analysis further showed how increasing the mass ratio increases the

Table 4.4: Results of the mass reduction analysis including what mass ratio for the optimal TID configuration produces the same reduction as the TMD configuration and the resulting saved mass

Mass Reduction Analysis							
Heave Free Decay				Pitch Free Decay			
	TMD	TID			TMD	TID	
% Reduction	μ	μ	Δ mass (kg)	% Reduction	μ	μ	Δ mass (kg)
18.92%	0.01	0.009	20402	13.17%	0.01	0.009	11256
25.22%	0.02	0.016	60642	18.07%	0.02	0.016	53466
29.29%	0.03	0.023	96098	21.53%	0.03	0.024	90329
32.24%	0.04	0.031	130710	24.22%	0.04	0.031	123394
34.55%	0.05	0.038	164900	26.41%	0.05	0.039	154911
36.43%	0.06	0.046	200216	28.25%	0.06	0.047	186005
38.02%	0.07	0.053	235954	29.82%	0.07	0.054	218366
39.38%	0.08	0.061	273521	31.19%	0.08	0.062	251712

performance gap between the TMD and optimal TID configurations. For the pitch free decay optimization, the optimal TID configuration operating at a mass ratio of 6.2%, produces the same reduction as the TMD configuration operating at a mass ratio of 8%, resulting in a mass reductions of over 250,000 kg. The performance gap is even further exaggerated for the heave free decay optimization, where the optimal TID configuration operating at a mass ratio of 6.1%, produces the same reduction as the TMD configuration operating at a mass ratio of 8%, resulting in a mass reductions of over 270,000 kg. Beyond the mass reduction analysis, the curve fit equations can also be used to predict the performance of the structural control methods at specific mass ratios driven by design requirements. Based on the analyses presented in this study, both methods of structural control can be considered a viable method for vibration reduction. Moreover, the optimal TID configuration provides an alternative control method that can produce similar reduction while saving mass or even greater reduction using the same mass.

4.3 Regular Wave Optimization

4.3.1 Regular Wave Optimization Setup

The regular wave optimization uses the same system properties presented in Table 3.9, and is conducted for a regular wave case representative of the environment where the system would be deployed. For this regular wave case, NREL's Marine Energy Atlas was used to estimate the wave conditions most common at proposed wind farm locations [40]. The sea state used has a wave period of 5 seconds and a wave height of 1.5 meters. The objective functions used for this analysis are identical to Equation 4.1. Though, it was found that reducing the heave RMS value also resulted in significant reductions for pitch, so only this objective function was used. Future studies could analyze whether reducing the pitch RMS value or both RMS values yields improved results. The RMS and percent reduction values analyzed in the following section are calculated using the same methods as the free decay optimization, equations 4.3 and 4.5 respectively. The regular wave optimization is conducted for a mass ratio of 3%, future studies could analyze the effects different mass ratios have on the reductions. The only additional parameter is the ramp time, t_{ramp}, which is set to $15 * (wave\, period)$. These values are chosen such that the regular sea state fully develops for the baseline case within a reasonable period of time.

4.3.2 Regular Wave Optimization Results

Figure 4.7 shows the optimized heave and pitch response of all configurations, where all structural control is operating with a mass ratio of 3%. The sinusoidal responses appear to be solid only because the responses are recorded for 5000 seconds. Such a long time range is chosen so that the response of all configurations has enough time to develop. If a zoomed in section of the plots were shown, the familiar sinusoidal response would still be evident. All responses show the benefit of adding the ramp function, the curves gradually increase all the way up until the ramp function. For the baseline case, the ramp function allows the response to cleanly reach equilibrium, whereas if a ramp was not used it may take 300 seconds or longer to reach equilibrium. The heave and pitch responses in figures 4.7a and 4.7b respectively, show the structural control configurations providing significant reductions compared to baseline. Furthermore, both figures also show the red response of the optimal TID configuration slightly outperforming the blue response of the traditional TMD configuration. Once again, the control parameters returned by the regular wave optimization are presented in the Appendix.

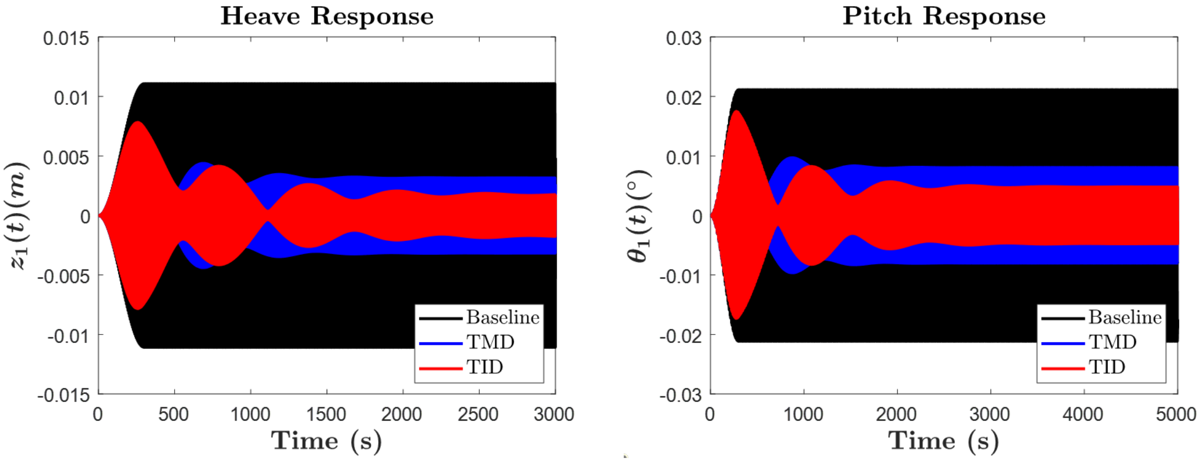

(a) Heave Response

(b) Pitch Response

Figure 4.7: Optimized heave and pitch time domain response for a representative sea state, using a mass ratio of 3%

The heave and pitch reduction results for the regular wave optimization are shown in tables 4.5. Table 4.5, shows the TMD providing significant reduction compared to baseline. For heave, the reductions are equal to 69.35% and 76.74% for the TMD and TID configurations, respectively. Moreover, the leftmost column points how much more reduction the TID configuration provides compared to the TMD. For heave, this improvement is +7.39%. The

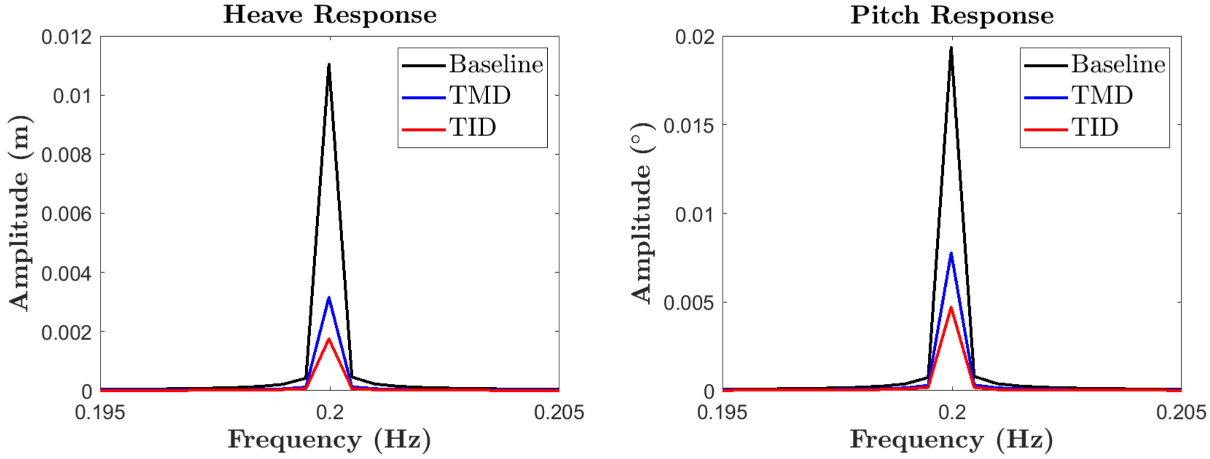

(a) Heave Response **(b)** Pitch Response

Figure 4.8: Optimized heave and pitch frequency domain response for a representative sea state, using a mass ratio of 3%

pitch reduction results in Table 4.5 tell a story very similar to the heave reduction results. Both configurations provide significant reduction in RMS value compared to baseline. The values are 57.77% and 68.19% for the TMD and TID configurations, respectively, with a performance improvement of 10.42%. Overall, the regular wave optimization further demonstrated the potential benefit of implementing structural control into the semisubmersible platform. The results also showed the potential improvement that can be provided by the inerter based structural control.

Table 4.5: Results of the regular wave optimization

Regular Wave Optimization						
	Baseline	Platform + TMD		Platform + TID		
DOF	RMS	RMS	% Reduction	RMS	% Reduction	Δ Reduction
Heave (m)	0.0077	0.0024	69.35%	0.0018	76.74%	7.39
Pitch (°)	0.0135	0.0057	57.77%	0.0043	68.19%	10.42

These results can also be visualized in the frequency domain using MATLAB's fast Fourier transform function. In this way, it is possible to see the systems amplitude for a range of different frequencies. The frequency domain responses, derived from the time domain response, are shown in Figure 4.8. These figures the control configurations effectively mitigating the systems response to the input wave period of 5 seconds. For both heave and pitch, the optimal TID configuration visually provides greater reduction compared to the TMD configuration.

4.4 Irregular Wave Analysis

In addition to the regular wave optimization, an irregular wave analysis is conducted, where a system using the same optimal parameters found during the regular wave optimization is excited using an irregular wave case. This irregular wave case uses the Bretschneider spectrum defined in Section 3.1, with a significant wave height and period equal to 1.5 meters and 5 seconds respectively. These wave properties are identical to the ones used for the regular wave optimization. This choice was intentional in order to see how the control configurations would perform for irregular wave excitation, when designed to limit the dominant wave frequency. The time domain results of this analysis are presented in Figure 4.9. Visually, this figure shows the blue line of the TMD and dashed red line of the TID configurations reducing the peaks of the baseline configuration. Figure 4.10 shows the pitch response for an extended time frame. This plot shows the fully developed behavior of the system and the results are largely the same as the previous figures. The blue and red line of the control configurations consistently produce smaller peaks then the black line of the baseline configuration. While the blue and red lines mostly overlap for reasons discussed in the following paragraph.

The percent reduction numbers related to this plot are shown in Table 4.6. For both degrees of freedom, the percent reduction is on the order of roughly 20%. Heave reduction values are equal to equal to 20.87% and 17.83% for the TMD and TID configurations respectively.

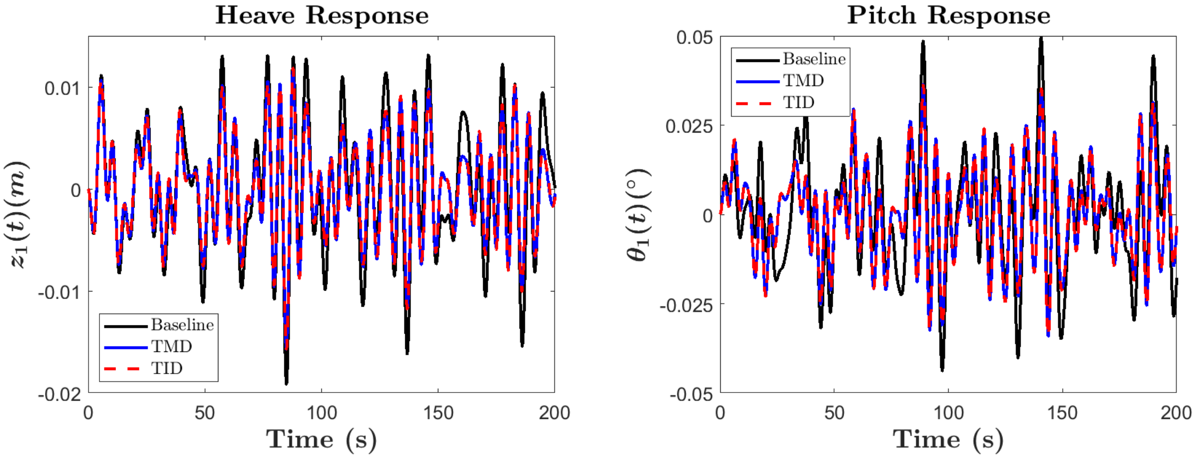

(a) Heave Response **(b)** Pitch Response

Figure 4.9: Heave and pitch time domain response for a representative irregular wave case, using a mass ratio of 3%

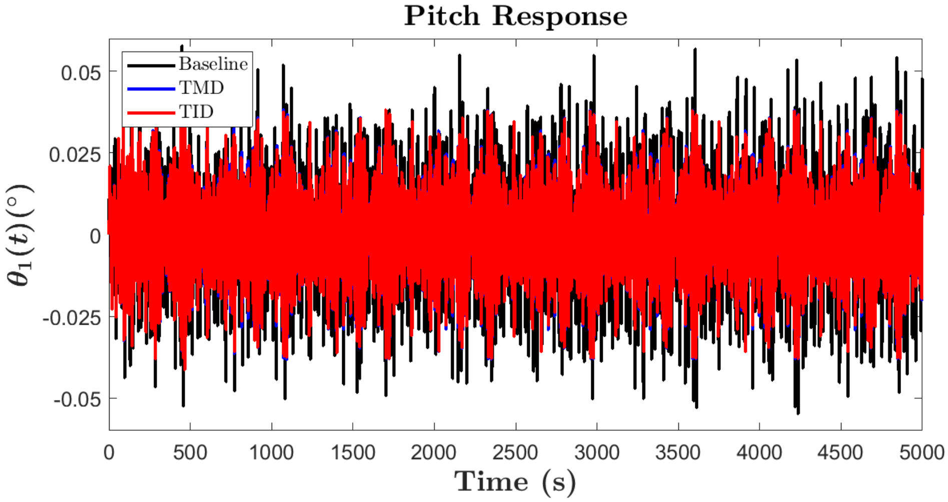

Figure 4.10: Pitch time domain response for a representative irregular wave case, using a mass ratio of 3%, ran for an extended period of time

Interestingly the TMD outperforms the TID, though that is likely due to the fact the values are optimized for the significant wave frequency and not the spectrum as a whole. If the another optimization was conducted where the RMS response to the irregular wave excitation was used as the objective function, it is likely that the TID would once again outperform the TMD configuration. The pitch reduction values are equal to roughly 22.20% for both the TMD and TID configurations. Overall, the performance of a system designed to reduce the significant wave frequency of an irregular wave spectrum provides meaningful reduction on the order of 20% for both heave and pitch. With the TMD slightly outperforming the TID because of the lack of final tuning, an irregular excitation based objective function would provide.

Table 4.6: Results of the irregular wave analysis

Irregular Wave Analysis					
	Baseline	Platform + TMD		Platform + TID	
DOF	RMS	RMS	% Reduction	RMS	% Reduction
Heave (m)	0.0067	0.0055	20.87%	0.0053	17.83%
Pitch (°)	0.0171	0.0133	22.20%	0.0133	22.20%

4.5 Hydrodynamic Coefficient Analysis

As discussed in Section 3.1, the hydrodynamic forces used in the following optimizations are derived using linear potential flow and are therefore, dependent on hydrodynamic coefficients. These coefficients are acquired from a BEM solver and are a function of wave frequency. Moreover, AQWA will return matrices of coefficients, where each row and column corresponds to a certain degree of freedom, and each matrix corresponds to a different wave frequency. For a regular wave case, it is most common to use hydrodynamic coefficients corresponding to the wave frequency. It is less common for this same approach to be used for free decay and irregular wave cases, given the influence of other frequencies inherent with these cases. It is more common to use a convolution integral approach to formulate the radiation damping force. This approach utilizes a radiation impulse response function to capture the effects of a range of frequencies, as well as system's velocity history in order to quantify how past motion influences future motion. However, this study opted to use the simplified method of selecting singular hydrodynamic coefficient values for free decay and irregular wave cases, for a number of reasons. The primary reason has to do with the requirement of a velocity history for the convolution method. It is difficult to keep a record of the systems velocity history within MATLAB given that the most widely used differential equation available are variable time step. Meaning that even if you are able to record the velocity value at each time step, the values would not correlate to the desired, input time step. A work around for this would be calling the differential equation solver for every single time step within a for loop, and manually saving the results to a velocity history. While this approach would work, it would drastically increase the time required for running simulations. And for a project that requires 100s if not 1000s of iterations of the model to be solved for each optimization, this would have had resulted in traditional optimization being borderline unfeasible. For this reason, the simplified approach for determining the hydrodynamic coefficients was adopted.

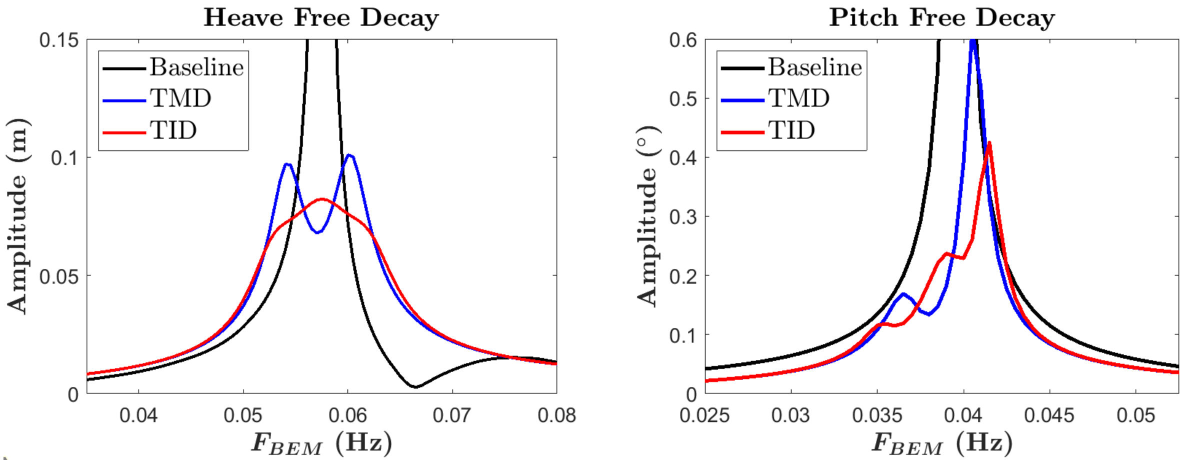

(a) Heave free decay **(b)** Pitch free decay

Figure 4.11: Results of the study analyzing how using different wave periods to determine the hydrodynamic coefficients affects the amplitude at the original wave period used

A study was conducted to visualize whether or not this simplified approach had a drastic effects on the results of the optimizations. For two free decay tests, a range of frequencies was used to determine the hydrodynamic coefficients. For each frequency used, it's corresponding amplitude was taken from the frequency domain response. In this way, the hydrodynamic coefficients are representative for each amplitude value recorded. Plotting these amplitudes as a function of the frequencies used to determine the hydrodynamic coefficients should result in an imperfect plot that resembles Figure 4.5. Figure 4.11, shows the results of this study. Where F_{BEM} is simply the wave frequency used to determine the hydrodynamic coefficients. These plots show similar shapes, natural frequencies, and amplitudes to Figure 4.5, from the earlier free decay section. Moreover, both control configurations are still shown outperforming the baseline, and the TID still outperforms the TMD as expected. Figure 4.12, plots the frequency domain response for a heave free decay test using the simplified hydrodynamics presented earlier and the method described in this section. ”TMD-S” refers to the simplified method, while the ”TMD-F” refers to the method used in this section. This figure shows the similarity between the two methods, with the TMD and TID cases matching up nicely. It is worth noting that ”Baseline-F” is expected to line up closer with ”TMD-F” and ”TID-F”, given the behavior of the other curves. The reasoning for this discrepancy can likely be contributed to the imperfection associated with this method for creating a frequency domain response. In order to further show why a difference exists between the two methods, a plot of the added mass and radiation damping for this frequency range is shown in Figure 4.13. This figure shows that the coefficients are in fact not constant, and fluctuate over the selected frequency range. These results show that while a convolution approach may be more optimal, this simplified hydrodynamic approach is suitable for a study whose focus is exploring the feasibility and performance of different control methods within an offshore floating wind platform through traditional optimization methods.

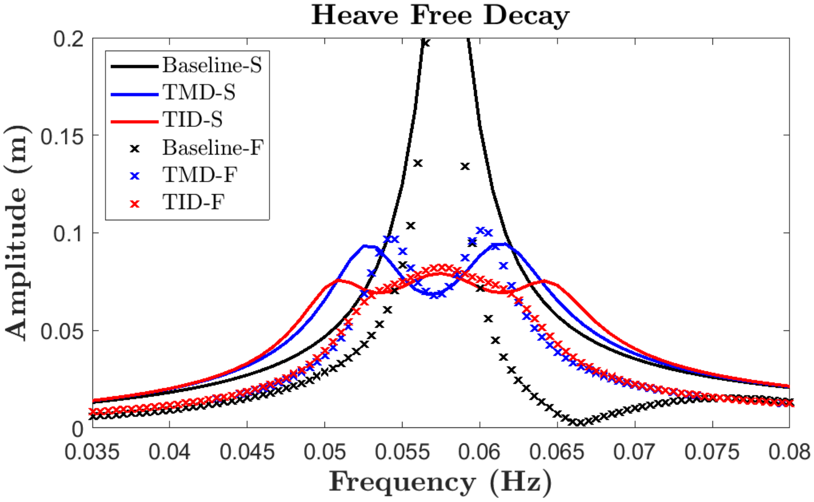

Figure 4.12: Frequency domain comparison between the two different methods for determining the hydrodynamic coefficients

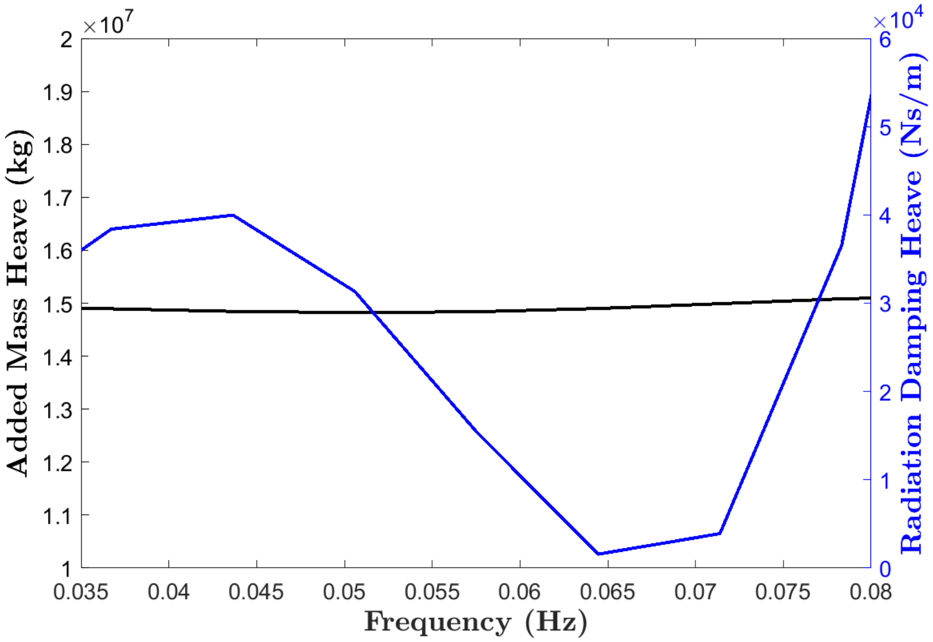

Figure 4.13: Hydrodynamics coefficients for the frequency range of Figure 4.11

Chapter 5

Conclusion and Future Work

5.1 Conclusion

This study has analyzed the potential benefits of implementing passive structural control systems into a semisubmersible offshore floating wind platform. These benefits include the reduction of the platform's heave and pitch response. The structural control systems studied includes a traditional TMD system, as well as an optimal inerter based control system. Three models were derived including a baseline model of just the semisubmersible supported wind turbine, a TMD model of the wind turbine plus three traditional TMDs located inside the three columns of the platform, and an optimal TID model of the wind turbine plus three optimal TIDs also located inside the columns of the platform. These models were verified by comparing results to identical WEC-Sim models for two free decay tests and one regular wave case. Optimization is incorporated into the models in order to determine whether these structural control methods can in fact provide reductions to the heave and pitch response, and if so, what parameters produce the greatest reduction. Optimizations were conducted for heave and pitch free decay tests and four different regular wave cases. And the optimal regular wave results were tested against irregular wave excitation. The key conclusions from these studies are as follows:

- The TMD and optimal TID configurations provided significant reductions to the free decay responses of the wind turbine, with reductions ranging from 20% to 40% for heave reduction and 13% to 34% for pitch reduction. Furthermore, the optimal TID outperforms the TMD at every mass ratio for both heave and pitch optimizations. This performance gap ranges from 1% at lower mass ratios to 4% at higher mass ratios.

- The percent reduction achieved from the TMDs and optimal TIDs appears to follow a logarithmic trend based on the curve fitting analysis conducted. The analysis once again shows the TID outperforming the TMD at all mass ratios, and shows this performance gap increasing as the mass ratio gets larger. The curve fitting results presented in this study could be used by designers in the future to estimate the percent reduction at any desired mass ratio.

- The curve fitting analysis also quantified how the optimal TID can provide the same reduction using smaller mass ratios, reducing the necessary physical mass in the process. For the heave reduction, the optimal TID reduces the necessary mass by as much as 270,000kg at the largest mass ratio. For pitch reduction, the necessary mass is reduced by over 250,000kg.

- The TMD and optimal TID control systems provided significant reductions for the heave and pitch response of the wind turbine under regular wave excitation. For heave, these reductions ranged from 69.35% for the TMD configuration and 76.74% for the TID configuration. For pitch, the reductions ranged from 57.77% for the TMD configuration and 68.19% for the TID configuration. The performance gap between the TMD and TID was +7.39% for heave and +10.42% for pitch.

- The TMD and optimal TID control systems provide meaningful reduction for irregular sea states when optimized for the input spectrum's significant wave frequency. The heave and pitch response for both configurations saw reductions of roughly 20%.

Based on these conclusions, it is clear that structural control can provide significant reductions to the heave and pitch responses of the semisubmersible floating offshore wind platform. In all studies, the traditional TMD provided meaningful reductions compared to baseline, while the optimal TID consistently outperformed the TMD. The use of the optimal TID configuration in the future will largely depend on whether designers are interested in either providing slightly more reduction at similar mass ratios, or reducing the necessary physical mass by providing similar reduction compared to the TMD at smaller mass ratios.

5.2 Future Work

While this study has performed several analyses regarding the implementation of various structural control subsystems into a semisubmersible floating offshore wind platform, these efforts could be continued by a few supplemental research topics. These research topics include:

- Implementing constant wind loading onto the system and performing additional optimizations
- Developing a convolution based formulation for radiation damping and added mass affects and analyzing the effects on the free decay optimization results. Moreover, one could implement drag damping into the models and analyze the effects on the optimization results.
- Studying the impact an additional TMD or TID added to the nacelle would have on heave and pitch reductions.
- Adding several other inerter based structural control configurations into the semisubmersible platform for added performance comparisons.

Appendices

Appendix A

Optimized Parameters

Table A.1: Table of optimal parameters for the heave free decay optimization

Optimal Parameters - Heave					
μ	$m_{2,3,4}$ (kg)	$k_{2,3,4}$ (N/m)	$c_{2,3,4}$ (Ns/m)	$k_{5,6,7}$ (N/m)	$b_{2,3,4}$ (kg)
TMD - 0.01	46,900	6,088	1,101	-	-
0.02	93,800	12,024	3,287	-	-
0.03	140,700	17,848	5,986	-	-
0.04	187,600	23,528	9,160	-	-
0.05	234,500	29,096	12,729	-	-
0.06	281,400	34,552	16,617	-	-
0.07	328,300	39,880	20,785	-	-
0.08	375,200	45,112	25,198	-	-
TID - 0.01	46,900	6,028	65	112	836
0.02	93,800	11,912	159	294	2,204
0.03	140,700	17,560	440	658	4,904
0.04	187,600	23,160	674	1,002	7,455
0.05	234,500	28,536	1,141	1,531	11,332
0.06	281,400	33,768	1,738	2,155	15,866
0.07	328,300	38,856	2,484	2,877	21,072
0.08	375,200	43,800	3,376	3,690	26,886

Table A.2: Table of optimal parameters for the pitch free decay optimization

Optimal Parameters - Pitch					
μ	$m_{2,3,4}$ (kg)	$k_{2,3,4}$ (N/m)	$c_{2,3,4}$ (Ns/m)	$k_{5,6,7}$ (N/m)	$b_{2,3,4}$ (kg)
TMD - 0.01	46,900	2,664	88	-	-
0.02	93,800	5,272	1,217	-	-
0.03	140,700	7,848	2,769	-	-
0.04	187,600	10,360	4,578	-	-
0.05	234,500	12,840	6,569	-	-
0.06	281,400	15,272	8,699	-	-
0.07	328,300	17,672	10,948	-	-
0.08	375,200	20,008	13,306	-	-
TID - 0.01	46,900	2,664	6	14	236
0.02	93,800	5,276	38	77	1,318
0.03	140,700	7,800	106	169	2,916
0.04	187,600	10,280	219	291	5,009
0.05	234,500	12,704	360	427	7,372
0.06	281,400	15,064	535	586	10,130
0.07	328,300	17,368	892	838	14,412
0.08	375,200	19,640	1,185	1,061	18,207

Table A.3: Table of optimal parameters for regular wave optimization with a mass ratio of 3%

Optimal Parameters - Regular Wave				
Control	$k_{2,3,4}$ (N/m)	$c_{2,3,4}$ (Ns/m)	$k_{5,6,7}$ (N/m)	$b_{2,3,4}$ (kg)
TMD	223,132	729	-	-
TID	222,016	55	747	466

Bibliography

[1] C. Draxl, A. Clifton, B.-M. Hodge, and J. McCaa, “The wind integration national dataset (wind) toolkit,” *Applied Energy*, vol. 151, pp. 355–366, 2015.

[2] W. Musial, P. Spitsen, P. Duffy, P. Beiter, M. Marquis, R. Hammond, and M. Shields, “Offshore wind market report: 2022 edition,” National Renewable Energy Lab.(NREL), Golden, CO (United States), Tech. Rep., 2022.

[3] Walt Musial. Overview of floating offshore wind. NREL. [Online]. Available: https://www.nrel.gov/news/video/overview-of-floating-offshore-wind-text.html

[4] A. N. Robertson and J. M. Jonkman, “Loads analysis of several offshore floating wind turbine concepts,” in *The twenty-first international offshore and polar engineering conference*. OnePetro, 2011.

[5] M. D. Esteban, J. J. Diez, J. S. López, and V. Negro, “Why offshore wind energy?” *Renewable energy*, vol. 36, no. 2, pp. 444–450, 2011.

[6] J. K. Kaldellis and D. Zafirakis, “The wind energy (r) evolution: A short review of a long history,” *Renewable energy*, vol. 36, no. 7, pp. 1887–1901, 2011.

[7] W. Musial, P. Spitsen, P. Beiter, P. Duffy, M. Marquis, A. Cooperman, R. Hammond, and M. Shields, “Offshore wind market report: 2021 edition,” EERE Publication and Product Library, Washington, DC (United States), Tech. Rep., 2021.

[8] B. Zhou, Z. Zhang, G. Li, D. Yang, and M. Santos, “Review of key technologies for offshore floating wind power generation,” *Energies*, vol. 16, no. 2, p. 710, 2023.

[9] I. Galparsoro, I. Menchaca, J. M. Garmendia, Á. Borja, A. D. Maldonado, G. Iglesias, and J. Bald, "Reviewing the ecological impacts of offshore wind farms," *npj Ocean Sustainability*, vol. 1, no. 1, p. 1, 2022.

[10] H. Farr, B. Ruttenberg, R. K. Walter, Y.-H. Wang, and C. White, "Potential environmental effects of deepwater floating offshore wind energy facilities," *Ocean & Coastal Management*, vol. 207, p. 105611, 2021.

[11] S. M. Maxwell, F. Kershaw, C. C. Locke, M. G. Conners, C. Dawson, S. Aylesworth, R. Loomis, and A. F. Johnson, "Potential impacts of floating wind turbine technology for marine species and habitats," *Journal of Environmental Management*, vol. 307, p. 114577, 2022.

[12] H. Díaz and C. G. Soares, "Review of the current status, technology and future trends of offshore wind farms," *Ocean Engineering*, vol. 209, p. 107381, 2020.

[13] J. Jonkman, "Definition of the floating system for phase iv of oc3," National Renewable Energy Lab.(NREL), Golden, CO (United States), Tech. Rep., 2010.

[14] J. Jonkman, S. Butterfield, W. Musial, and G. Scott, "Definition of a 5-mw reference wind turbine for offshore system development," National Renewable Energy Lab.(NREL), Golden, CO (United States), Tech. Rep., 2009.

[15] D. Matha, "Model development and loads analysis of an offshore wind turbine on a tension leg platform with a comparison to other floating turbine concepts: April 2009," National Renewable Energy Lab.(NREL), Golden, CO (United States), Tech. Rep., 2010.

[16] A. Robertson, J. Jonkman, M. Masciola, H. Song, A. Goupee, A. Coulling, and C. Luan,

"Definition of the semisubmersible floating system for phase ii of oc4," National Renewable Energy Lab.(NREL), Golden, CO (United States), Tech. Rep., 2014.

[17] National Renewable Energy Laboratory. (2005) Fast. [Online]. Available: https://www.nrel.gov/wind/nwtc/fast.html

[18] C. Pastia, S. G. Luca, F. Chira, and V. O. Roşca, "Structural control systems implemented in civil engineering," *Bulletin of the Polytechnic Institute of Jassy, Construction. Architecture Section*, pp. 76–80, 2005.

[19] H. Frahm, "Device for damping vibrations of bodies." Apr. 18 1911, uS Patent 989,958.

[20] S. Elias and V. Matsagar, "Research developments in vibration control of structures using passive tuned mass dampers," *Annual Reviews in Control*, vol. 44, pp. 129–156, 2017.

[21] M. Gutierrez Soto and H. Adeli, "Tuned mass dampers," *Archives of Computational Methods in Engineering*, vol. 20, pp. 419–431, 2013.

[22] M. C. Smith, "Synthesis of mechanical networks: the inerter," *IEEE Transactions on automatic control*, vol. 47, no. 10, pp. 1648–1662, 2002.

[23] I. Lazar, S. Neild, and D. Wagg, "Inerter-based vibration suppression systems for laterally and base-excited structures," in *Proceedings of EURODYN 2014*. Sheffield, 2014, pp. 1525–1530.

[24] L. Marian and A. Giaralis, "Optimal design of a novel tuned mass-damper–inerter (tmdi) passive vibration control configuration for stochastically support-excited structural systems," *Probabilistic Engineering Mechanics*, vol. 38, pp. 156–164, 2014.

[25] Y. Hu and M. Z. Chen, "Performance evaluation for inerter-based dynamic vibration absorbers," *International Journal of Mechanical Sciences*, vol. 99, pp. 297–307, 2015.

[26] Dr. Matthew Lackner at the University of Massachusetts Amherst & National Renewable Energy Laboratory. (2013) Fast-sc. [Online]. Available: https://www.umass.edu/windenergy/research/software/fastsc

[27] M. A. Lackner and M. A. Rotea, “Passive structural control of offshore wind turbines,” *Wind energy*, vol. 14, no. 3, pp. 373–388, 2011.

[28] Y. Si, H. R. Karimi, and H. Gao, “Modelling and optimization of a passive structural control design for a spar-type floating wind turbine,” *Engineering structures*, vol. 69, pp. 168–182, 2014.

[29] G. M. Stewart, “Load reduction of floating wind turbines using tuned mass dampers,” 2012.

[30] T. Li, Z. Liu, S. Liu, Y. Fan, Q. Yang, and H. Xiao, “Numerical study on passive structural control of semi-submersible floating wind turbine considering non-collinear wind and waves,” *Ocean Engineering*, vol. 266, p. 112745, 2022.

[31] D. Han, W. Wang, X. Li, and X. Su, “Optimization design of multiple tuned mass dampers for semi-submersible floating wind turbine,” *Ocean Engineering*, vol. 264, p. 112536, 2022.

[32] M.-A. Xue, P. Dou, J. Zheng, P. Lin, and X. Yuan, “Pitch motion reduction of semisubmersible floating offshore wind turbine substructure using a tuned liquid multicolumn damper,” *Marine Structures*, vol. 84, p. 103237, 2022.

[33] Y. Hu, J. Wang, M. Z. Chen, Z. Li, and Y. Sun, “Load mitigation for a barge-type floating offshore wind turbine via inerter-based passive structural control,” *Engineering Structures*, vol. 177, pp. 198–209, 2018.

[34] S. Sarkar and B. Fitzgerald, “Fluid inerter for optimal vibration control of floating offshore wind turbine towers,” *Engineering Structures*, vol. 266, p. 114558, 2022.

[35] R. Ma, K. Bi, and H. Hao, “Heave motion mitigation of semi-submersible platform using inerter-based vibration isolation system (ivis),” *Engineering structures*, vol. 219, p. 110833, 2020.

[36] C. Lee and J. Newman, *WAMIT User Manual*, WAMIT Inc., Chestnut Hill, MA, 4 2013. [Online]. Available: https://www.wamit.com/manualupdate/history/V70_manual_old.pdf

[37] National Renewable Energy Laboratory and National Technology & Engineering Solutions of Sandia, LLC (NTESS). (2022) Theory manual. [Online]. Available: https://wec-sim.github.io/WEC-Sim/master/theory/theory.html#id36

[38] D. Morin, *"Introduction to Classical Mechanics With Problems and Solutions"*. "Cambridge University Press", 2008, ch. 6.

[39] N. R. E. Laboratory and L. N. National Technology & Engineering Solutions of Sandia, “Wec-sim,” https://github.com/WEC-Sim/WEC-Sim, 2022.

[40] National Renewable Energy Laboratory. (2021) Marine energy atlas. [Online]. Available: https://maps.nrel.gov/marine-energy-atlas/